

On the geometry of aggregate snowflakes

Axel Seifert*

Deutscher Wetterdienst, Offenbach, Germany

Fabian Jakub

Deutscher Wetterdienst, Offenbach, Germany

Christoph Siewert

Deutscher Wetterdienst, Offenbach, Germany

Leonie von Terzi

Ludwig-Maximilians University of Munich, Munich, Germany

Stefan Kneifel

Ludwig-Maximilians University of Munich, Munich, Germany

Abstract

Snowflakes play a crucial role in weather and climate. A significant portion of precipitation that reaches the surface originates as ice, even when it ultimately falls as rain. Contrary to the popular image of symmetric, dendritic crystals, most large snowflakes are irregular aggregates formed through the collision of primary ice crystals, such as hexagonal plates, columns, and dendrites. These aggregates exhibit complex, fractal-like structures, particularly at large sizes. Despite this structural complexity, each aggregate snowflake is unique, with properties that vary significantly around the mean — variability that is typically neglected in weather and climate models. Using a physically based aggregation model, we generate millions of synthetic snowflakes to investigate their geometric properties. The resulting dataset reveals that, for a given monomer number (cluster size) and mass, the maximum dimension follows approximately a lognormal distribution. We present a parameterization of aggregate geometry that captures key statistical properties, including maximum dimension, aspect ratio, cross-sectional area, and their joint correlations. This formulation enables a stochastic representation of aggregate snowflakes in Lagrangian particle models. Incorporating this variability improves the realism of simulated fall velocities, enhances growth rates by aggregation, and broadens Doppler radar spectra in closer agreement with observations.

1 Introduction

Snowflakes have fascinated scientists for centuries, dating back to the 17th century when German astronomer Johannes Kepler first speculated on the physics behind their hexagonal shapes (Ball, 2011). He proposed that the hexagonal geometry of snowflakes might be explained by a close packing of spheres — an idea that led to what is now known as Kepler’s conjecture (Hales, 2024). Today, we understand that the intricate shape of dendritic snow crystals arises from the hexagonal molecular structure of ice, combined with the Mullins–Sekerka instability that promotes the growth of filament-like branches (Libbrecht, 2019). However, most snowflakes observed in the atmosphere are not pristine dendritic crystals but rather aggregates of primary ice crystals formed through collisions. These

*Corresponding author: axel.seifert@dwd.de

primary ice crystals — or monomers — may be hexagonal plates, columns, or dendrites. The resulting aggregate snowflakes are structurally complex and exhibit fractal scaling behavior when composed of many monomers, particularly at large cluster sizes (Westbrook et al., 2004a,b). In weather and climate models, and even in the most detailed cloud-resolving models, snowflake geometry is usually prescribed using empirical relations and simple power-law fits (e.g., Mitchell et al., 1990; Mitchell, 1996). Yet measurements of the mass–size relationships for aggregates consistently show substantial scatter around the mean. This variability is evident in both classic studies (Locatelli and Hobbs, 1974; Mitchell et al., 1990) and more recent measurements using high-resolution imaging and machine learning (Leinonen et al., 2021). Importantly, this scatter cannot be fully explained by measurement error alone. To a large extent, it is a reflection of natural variability in aggregate snowflake geometry. For a given mass and monomer number, aggregate snowflakes can vary from compact and nearly spherical to chain-like and highly elongated. This geometric diversity directly affects particle properties such as terminal fall velocity: more compact aggregates fall faster than elongated ones of the same mass. Since snowflake growth via aggregation is largely driven by differential sedimentation, variations in fall velocity can enhance the growth rate. This effect is similar to atmospheric turbulence leading to an increase in the collision rate by introducing variability in the particle velocity (Shaw, 2003; Grabowski and Wang, 2013; Onishi and Seifert, 2016; Chellini and Kneifel, 2024).

Given these implications, it is important to characterize not only the mean behavior of snowflakes but also the statistical variability of their geometry. Specifically, we investigate the probability distribution governing deviations in maximum dimension for a given mass and monomer number. This leads to the development of a stochastic model for aggregate snowflake geometry, suitable for use in Lagrangian Monte Carlo particle simulations of cloud microphysics. Decades after the pioneering work of Telford (1955) and Gillespie (1975), Lagrangian particle-based models have gained renewed interest and offer new opportunities to address longstanding challenges in cloud physics (Shima et al., 2009; Brdar and Seifert, 2018; Morrison et al., 2020; Shima et al., 2020; Chandrakar et al., 2021; Welss et al., 2024; Morrison et al., 2024).

Previous studies of aggregate snowflake geometry, including those by Dunnavan et al. (2019), Dunnavan (2021), and Przybylo et al. (2022), have examined snowflake shape, density, and fall speed using observational datasets and Monte Carlo aggregation models. Dunnavan et al. (2019) employed bivariate statistical methods to show how monomer habit and aggregation history influence the observed geometric variability. Przybylo et al. (2022) expanded on this by using the Ice Particle and Aggregate Simulator (IPAS) to generate a large database of computer-simulated aggregates, aimed at informing bulk microphysical parameterizations. Dunnavan (2021) focused on how variability in snowflake geometry affects terminal fall velocity, a process that is revisited in this study. While these studies offer important insights, their statistical frameworks are not readily applicable in Lagrangian particle models (LPMs). To address this, we develop a stochastic parameterization tailored for use in LPMs. In this approach, key geometric properties such as maximum dimension, aspect ratio, and cross-sectional area are probabilistically sampled based on three inputs: ice mass, monomer number, and monomer habit. This allows for efficient and physically consistent generation of snowflake geometries, supporting both LPMs and remote sensing forward operators.

The paper is organized as follows: Section 2 introduces the aggregation model and the dataset that underpins our parameterization. Section 3 describes the statistical model of snowflake geometry, focusing on maximum dimension, aspect ratio, and projected area, derived as functions of mass, monomer number, and habit. In Section 4, we demonstrate the implementation of this parameterization within the Lagrangian particle model McSnow. In Section 5 we investigate the influence of the new parameterization on common radar variables, also introducing a new scattering database developed for this study. Section 6 concludes with a summary and outlook.

2 Aggregation modeling

The aggregation model described by Leinonen and Szyrmer (2015) and Leinonen and Moisseev (2015) constructs three-dimensional representations of aggregate snowflakes by combining primary crystals of predefined shapes such as hexagonal columns, plates, or dendrites. This approach is conceptually similar to the model presented by Westbrook et al. (2004a,b). Our analysis focuses exclusively on unrimed snowflakes, although the geometry of rimed aggregates has been addressed in previous work (Seifert et al., 2019). The same aggregation framework has also been used to study the physical properties of snowflake aggregates (Karrer et al., 2020), their scattering characteristics (Ori et al., 2021), and to develop retrieval algorithms based on in-situ observations (Leinonen et al., 2021). In addition, the model has been applied to generate 3D-printed snowflake analogs for laboratory experiments (Köbschall et al., 2023).

Building on this framework, we refine the constant penetration depth concept introduced by Leinonen and Moisseev (2015) to allow the formation of slightly more compact aggregates. The basic implementation for attaching monomers and aggregates follows a procedure similar to the game *Tetris*. Two particles are randomly aligned in the vertical direction such that their horizontal, axis-aligned bounding boxes overlap. The lower one is then moved upward until it intersects the upper one at the point of minimum vertical distance. If no intersection occurs, the orientation is randomized again until contact is achieved. This method, however, tends to produce very fragile connections, comparable to two needles just touching at their tips, resembling the near-touching fingers in Michelangelo's *The Creation of Adam*.

To increase the compactness of the aggregates, the original approach extended the contact depth by a fixed amount. Once a contact point was found, the lower particle was moved an additional $80\text{ }\mu\text{m}$ upward. Although this adjustment led to denser structures on average, it also introduced unphysical side effects, sometimes producing disconnected or overly porous aggregates, particularly for small particles. In our revised approach, we aim to improve the realism of the intersection process by excluding the outer portion of a particle's volume during contact evaluation. Specifically, we define a spherical boundary that encloses 50 % of the particle's material volume and consider only the inner region for collision detection. For needle-shaped monomers, this effectively removes the tips from consideration and reduces the usable intersection area by about one quarter. For plates, halving the usable volume corresponds to excluding approximately $1 - 1/\sqrt{2} \approx 29\text{ \%}$ of the diameter. For a sphere, the excluded fraction becomes $1 - 1/\sqrt[3]{2} \approx 20\text{ \%}$. In a more extreme case, such as a compact ice sphere with a long protruding arm, the arm would be excluded entirely from the intersection calculation. Finally, to avoid excessive exclusion in large particles, we cap the masked region to a maximum shell thickness of $120\text{ }\mu\text{m}$.

Primary crystals are drawn from a truncated exponential size distribution, with a minimum size of $\bar{D}_{\text{ice}}/4$ and a maximum of $100\bar{D}_{\text{ice}}$, where \bar{D}_{ice} is the mean monomer size, ranging from $50\text{ }\mu\text{m}$ to $500\text{ }\mu\text{m}$. The aggregation model operates at a finite spatial resolution, which in our study is proportional to the mean monomer size and defined as $\Delta = \bar{D}_{\text{ice}}/20$. Monomer habits include needles, plates, rosettes, and dendrites. For details on the monomer geometries, see Figure 1 of Leinonen and Moisseev (2015). In this work, we restrict our attention to aggregates composed of needles, plates, and dendrites.

To generate a comprehensive dataset, random samples are created with monomer numbers N ranging from 2 to 2048, and mean monomer sizes \bar{D}_{ice} from $50\text{ }\mu\text{m}$ to $500\text{ }\mu\text{m}$. We produce five distinct datasets: (1) needles only, (2) plates only, (3) dendrites only, (4) mixtures of needles and plates, and (5) mixtures of needles and dendrites. Following the terminology of Mitchell (1996), we refer to these as aggregates of mixtures, meaning that individual aggregates contain monomers of different shapes. The monomer ratio MR denotes the number fraction of needle monomers, with the remainder being

plates (or dendrites).

In our datasets, the aggregates of mixtures combine prolate forms, such as needles, with oblate ones, such as plates or dendrites. This choice is motivated by habit predictions in Lagrangian particle models, in particular McSnow, and also by the possibility that fragmentation introduces needle-shaped monomers into regions where dendritic growth occurs. While other combinations, like plate–dendrite mixtures, may form in nature, they are not considered here. Each single-habit dataset contains approximately one million samples, while the mixed-habit datasets include about five million samples each to cover a wide range of habit ratios.

For each aggregate, the database records several properties: the number of monomers N , the mean monomer size \bar{D}_{ice} , the total mass m , the maximum dimension D , the vertically projected cross-sectional area A , and three characteristic lengths L_x , L_y , and L_z , which represent the maximum extent of the aggregate along the respective spatial axes. After every collision, a principal axis transformation is performed. As a result, the ordering $L_x > L_y > L_z$ holds for nearly all particles. However, a few exceptions with $L_x < L_y$ occur due to the geometry of the principal axis transformation. Although the dataset includes the principal axes, these are not used in the subsequent analysis.

The horizontal aspect ratio, defined as $\phi_{xy} = L_x/L_y$, is relevant for estimating terminal fall velocity, whereas the vertical aspect ratio, $\phi_{xz} = L_z/L_x$, is, for example, accessible through video disdrometer observations. For consistency with previous studies (Seifert et al., 2019; Karrer et al., 2020), the maximum dimension D_{max} is defined as the diameter of the smallest sphere that completely encloses the aggregate. While D_{max} and L_x are typically very similar, they are not identical.

3 Snowflake geometry

The fractal geometry of snowflakes is traditionally described using power-law relationships for both the mass–size and mass–area dependencies (Locatelli and Hobbs, 1974; Mitchell et al., 1990; Mitchell, 1996). Figure 1 shows the mass–size relations for aggregates of needles, aggregates of plates, and aggregates of dendrites. For monomer numbers greater than 10, the aggregate mass m scales with the maximum dimension D_{max} via a fractal exponent p as $m \propto D_{\text{max}}^p$.

In this study, we find exponents ranging from 2.03 for aggregates of needles, 2.08 for aggregates of dendrites, to 2.12 for aggregates of plates. The power law fit uses only samples with $D_{\text{max}} > 0.5$ mm and $N > 5$. It is important to note that the power-law fit describes only the mean behavior; a significant scatter around the mean is evident in Figure 1. In the following, we aim to understand and quantify this variability in more detail.

3.1 Maximum dimension

For a more detailed geometric model of aggregate snowflakes, the maximum dimension is normalized using the mean monomer diameter, denoted as \bar{D}_{mono} . This mean monomer diameter is derived from the aggregate mass m and the monomer number N using

$$\bar{D}_{\text{mono}} = \left(\frac{m}{a_i N} \right)^{1/b_i}, \quad (1)$$

where a_i and b_i are the parameters of the mass–size relation for the monomers (primary crystals). For needles these are $a_0 = 0.005$ and $b_0 = 1.89$, for plates $a_1 = 0.788$ and $b_1 = 2.48$, and for dendrites $a_2 = 0.013$ and $b_2 = 2.1$ with m in kg and \bar{D}_{mono} in m.

It is important to note that \bar{D}_{mono} differs from \bar{D}_{ice} . The former is specific to an individual aggregate, while the latter represents the mean of the monomer size distribution for an ensemble of particles as assumed in the aggregation model. With current observational techniques, \bar{D}_{mono} is

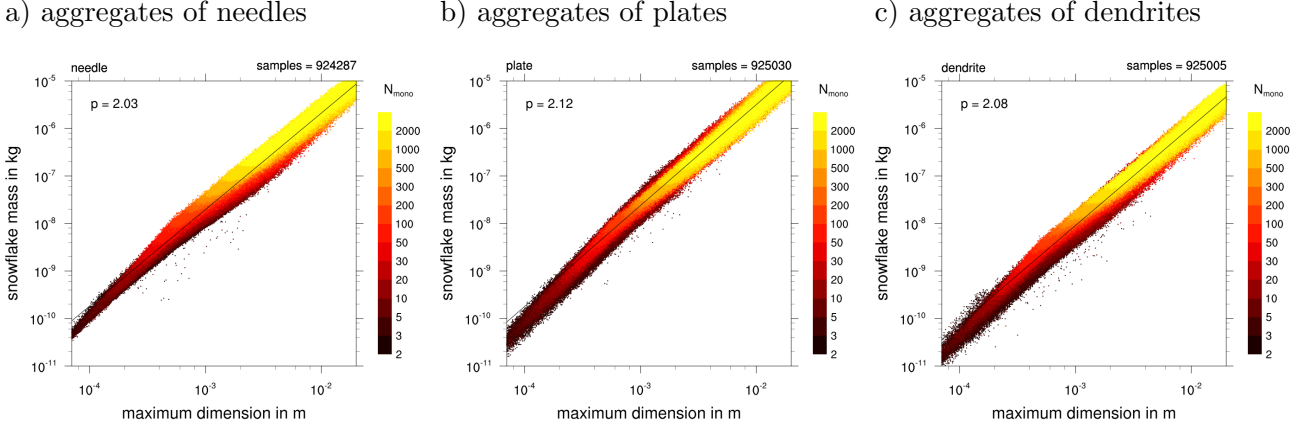


Figure 1: Scatter plots showing the mass-size relations for aggregates of needles, plates, and dendrites. Colors indicate monomer number N , and the regression line represents the power-law fit with fractal exponent p for $N > 5$.

generally not accessible via direct measurements but can be readily computed in a Lagrangian particle model.

The maximum dimension is made nondimensional using

$$\hat{D}_{\max} = \frac{D_{\max} - D_{\min}}{\bar{D}_{\text{mono}}}, \quad (2)$$

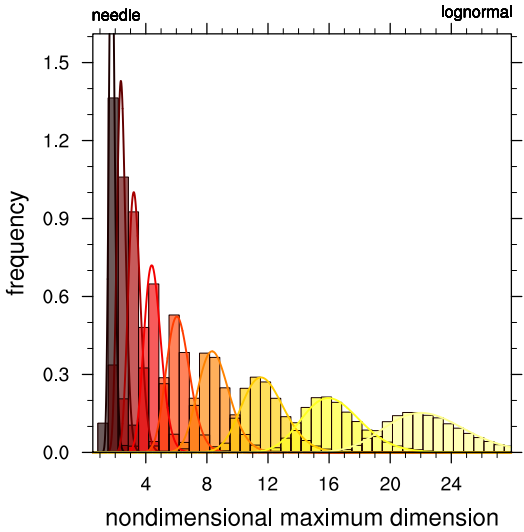
where $D_{\min} = 15 \mu\text{m}$ is a finite-size correction required due to the truncated exponential distribution of the aggregation model. Figure 2 presents histograms of \hat{D}_{\max} for various monomer numbers N . For a fixed N , the nondimensional maximum dimension \hat{D}_{\max} is approximately lognormally distributed.

To assess this approximation, statistical tests, including the Kolmogorov–Smirnov (KS) test and the Anderson–Darling (AD) test, were used to evaluate the goodness-of-fit to a lognormal distribution. Both tests were applied to subsets of 500 samples for various monomer numbers N . For all $N > 2$, the KS test did not reject the null hypothesis that the data follow a lognormal distribution at the 5 % significance level. However, the AD test, which is more sensitive to deviations in the tails of the distribution, rejected the null hypothesis for all values of N . These results suggest that while the lognormal distribution provides a reasonable approximation, it may not fully capture the true underlying distribution.

An alternative would be to apply the beta distribution, as in Dunnavan et al. (2019), which has the advantage of having bounded support, making it well-suited for modeling normalized geometric quantities such as D_{norm} or ϕ that are naturally restricted to finite intervals. This can help avoid unphysical values and better constrain the distribution’s tails compared to the lognormal. Here, we retain the lognormal distribution for its simplicity and computational efficiency. In practice, generating lognormal random variates is considerably faster than for the beta distribution: it requires only a single normal variate and an exponential transform. In contrast, sampling from the beta distribution often involves more complex rejection sampling or transformations of gamma-distributed variables. Given the high sample volume required in Lagrangian Monte Carlo models, this performance difference can be substantial.

The approximately lognormal shape of the aggregate size distribution observed in this study can be understood as a natural consequence of stochastic growth processes with bounded inputs. Similar statistical behavior has been reported in astrophysics, where the Stellar Initial Mass Function (IMF) is often modeled as a lognormal distribution at low and intermediate stellar masses, transitioning to a power-law tail at higher masses (Chabrier, 2003; Basu and Jones, 2004). This form arises from

a) aggregates of needles



b) aggregates of plates

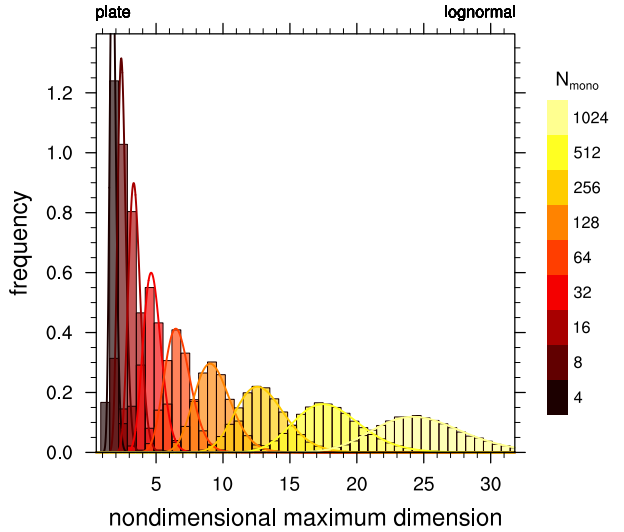


Figure 2: Histograms of the nondimensional maximum dimension \hat{D}_{\max} for aggregates of needles and aggregates of plates for different monomer numbers N . Solid lines represent lognormal distributions with the same mean and standard deviation as the data. The dendrite dataset looks similar and is not shown.

turbulent fragmentation and stochastic accretion, both of which resemble bounded multiplicative processes where initial conditions come from a limited distribution and growth proceeds via variable-length aggregation constrained by physical limits. The resulting IMF shows a lognormal core with deviations in the tails. This pattern is mirrored in the synthetic data from our snowflake aggregation model, where monomer sizes follow a truncated exponential distribution and growth obeys a fractal scaling law. Deviations from pure lognormality, especially in the tails, are therefore not artifacts, but natural consequences of the underlying physical constraints.

Next, we parameterize the mean and standard deviation of these lognormal distributions as functions of N . A power-law ansatz suffices for the mean of \hat{D}_{\max} consistent with a universal fractal scaling of aggregates (Westbrook et al., 2004a,b). This leads us to define another normalized maximum dimension:

$$D_{\text{norm}} = \hat{D}_{\max} \left(\frac{N_0}{N} \right)^\eta = \frac{D_{\max} - D_{\min}}{\bar{D}_{\text{mono}}} \left(\frac{N_0}{N} \right)^\eta, \quad (3)$$

such that $D_{\text{norm}} = 1$ corresponds to the mean aggregate snowflake, independent of N . For η we find 0.456 for aggregates of needles, 0.474 for aggregates of plates, and 0.457 for aggregates of dendrites. For aggregates of mixtures we find 0.459 for both the 50/50 mixture of needles and plates, and the 50/50 mixture of needles and dendrites. The corresponding values for N_0 are 1.136 for needles, 1.230 for plates, 1.161 for dendrites, 1.156 for the 50/50 mixture of needles and plates, and 1.152 for the needles and dendrite mixture. Note that with $D_{\text{norm}} = 1$, Eq. (3) results in a power-law for the mean mass-size relation.

Snowflakes with $D_{\text{norm}} > 1$ tend to be more elongated and chain-like, while those with $D_{\text{norm}} < 1$ are more compact and spherical. Figures 3 and 4 illustrate examples of aggregates with $D_{\text{norm}} < 1$, $D_{\text{norm}} \approx 1$, and $D_{\text{norm}} > 1$ for plate, needle and dendrite monomers at different values of N . These visualizations suggest an intuitive explanation for the lognormal shape of the D_{norm} distribution. Aggregates with $D_{\text{norm}} \approx 0.7$ are already nearly spherical, with aspect ratios close to one, and thus values much smaller than this are physically implausible. In contrast, for $D_{\text{norm}} > 1$, values exceeding 1.5 are common, and the most extreme, chain-like aggregates can reach up to $D_{\text{norm}} \approx 2$. This

asymmetry, with bounded compactness on one side and a broader range of elongation on the other, leads to a right-skewed distribution, reflecting the underlying geometric constraints.

For aggregates of needles we find that the standard deviation increases with N as shown in Figure 5 and saturates for large N . The functional dependency can be parameterized with:

$$\sigma_0 = 0.121 - 0.032 \frac{2}{N}. \quad (4)$$

For aggregates of plates the standard deviation shows no clear trend but oscillates around

$$\sigma_1 = 0.142, \quad (5)$$

which is the mean of the data for $N > 10$ (Fig. 5a). For aggregate of dendrites in Fig. 5b we find that the standard deviation decreases slowly with N following

$$\sigma_2 = 0.120 + 0.011 \left(\frac{50}{N} \right)^{0.35} \quad (6)$$

For aggregates of mixtures, the standard deviation is generally larger for small N compared to aggregates of only a single habit. This is because the different monomer geometries allow for more variability and, hence, higher standard deviations. The standard deviation then decreases monotonically with N . The following parameterization describes the data for mixture aggregates of 50 % needles and 50 % plates (Fig. 5a):

$$\sigma_{\frac{1}{2}}^{\circ} = 0.120 + 0.016 \left(\frac{50}{N} \right)^{0.4} \quad (7)$$

and similarly for aggregates of 50 % needles and 50 % dendrites (Fig. 5b).

$$\sigma_{\frac{1}{2}}^{*} = 0.120 + 0.015 \left(\frac{50}{N} \right)^{0.5}. \quad (8)$$

Small aggregates with a mixture of needles and dendrites have the largest standard deviation in this dataset.

3.2 Aspect ratio

Aggregate snowflakes are inherently anisotropic; their aspect ratio depends on both the monomer shape and monomer number N . In addition, the aspect ratio ϕ is correlated with the normalized maximum dimension D_{norm} , as can already be seen in Figs. 3 and 4. Westbrook et al. (2004a,b) showed that the mean aspect ratio of aggregate snowflakes approaches an asymptotic value of 0.65 for large N in their data. This asymptotic value is independent of the monomer shape. Figure 6 confirms their finding, but with a slightly larger asymptotic value of 0.74 in our data, suggesting more compact growth in our model at large N . This discrepancy may be due to differences in the aggregation model, such as grid resolution and, in particular, the concept of a penetration depth in our model, which may allow for more compact growth compared to that in Westbrook et al. (2004a,b). The main difference, however, is that Westbrook et al. define the aspect ratio as an average over random projections including the vertical axis resulting in a smaller absolute value.

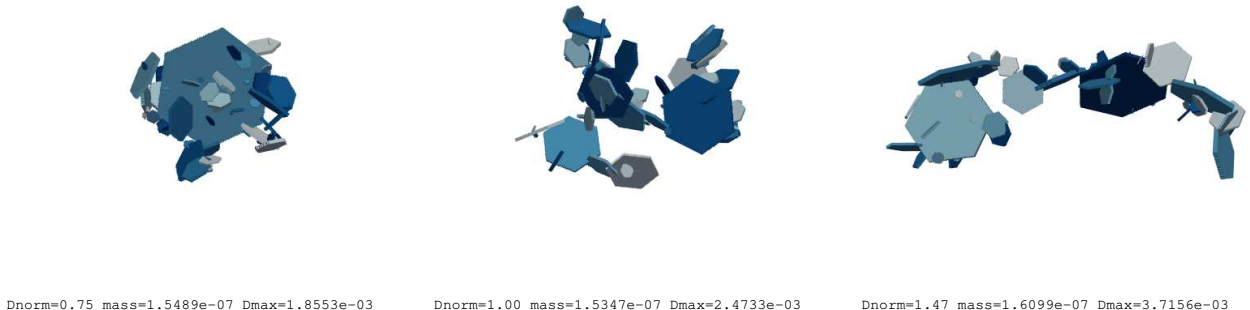
As expected from the aspect ratios of their respective monomers, aggregates of plates begin with a mean aspect ratio close to 0.9 (plates have a horizontal aspect ratio of one), with the aspect ratio decreasing monotonically with N toward 0.73 (Fig. 6a). In contrast, aggregates of needles start around 0.5, with ϕ increasing monotonically with N . For aggregates of needles the relation for the mean aspect ratio as a function of N can be parameterized with:

$$\phi_0(N) = 0.742 - 0.227 \left(\frac{2}{N} \right)^{0.95} \quad (9)$$

a) aggregates of needles with $N = 64$



b) aggregates of plates with $N = 64$



c) aggregates of dendrites with $N = 64$



Figure 3: Examples of aggregates of needles, aggregates of plates and aggregates of dendrites for monomer number $N = 64$ and different D_{norm} . For each aggregate, the normalized diameter D_{norm} , the mass m in kg, and the maximum dimension D_{max} in m is given. The snowflakes with $D_{\text{norm}} < 1$ (left column) are much smaller in terms of maximum dimension D_{max} than the elongated snowflakes with $D_{\text{max}} > 1$ (right column). The central column shows an example of the mean aggregates snowflake with $D_{\text{norm}} = 1$ for the given N . The aggregate mass m in each row is similar, but not identical.

a) aggregates of needles with $N = 1024$



b) aggregates of plates with $N = 1024$

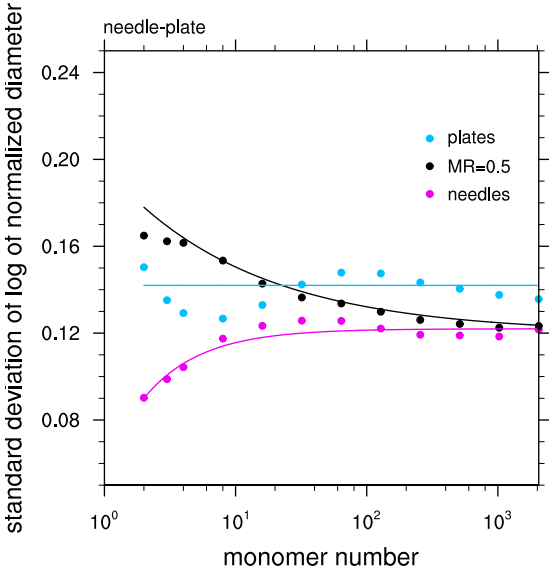


c) aggregates of dendrites with $N = 1024$



Figure 4: As Figure 3, but for a monomer number of $N = 1024$.

a) aggregates of needles and plates



b) aggregates of needles and dendrites

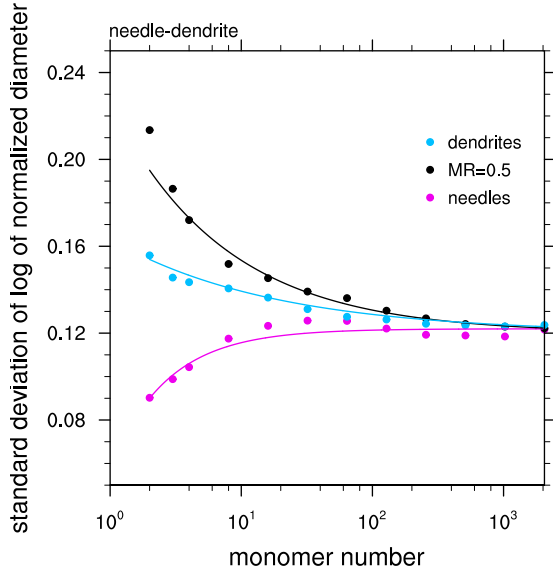


Figure 5: Standard deviation of the normalized diameter D_{norm} as a function of monomer number N for aggregates of plates, aggregates of needles, and mixture aggregates of plates and needles (left), and aggregates of needles, aggregates of dendrites, and mixture aggregates of both (right). Aggregates of mixtures are shown for different monomer ratios MR . The solid lines are the parameterizations using Eqs. (4)–(8).

and for plates aggregates with

$$\phi_1(N) = 0.736 + 0.141 \left(\frac{2}{N} \right)^{0.65} \quad (10)$$

The data of the 50/50 mixture aggregates of needles and plates follow the non-monotonic relation

$$\phi_{\frac{1}{2}}^{\circ}(N) = \begin{cases} 0.751 - 0.0456 \left(\frac{2}{N} \right)^{1.5}, & \text{for } N < 32, \\ 0.733 + 0.0186 \left(\frac{32}{N} \right)^{0.3}, & \text{otherwise.} \end{cases} \quad (11)$$

For other values of MR , linear interpolation between these three relations provides a sufficiently good approximation.

For aggregates of dendrites and the mixture of needles and dendrites the aspect ratio behaves very similar to the plate case. The only difference is that at low N aggregates of dendrites have a slightly larger standard deviation than aggregates of plates. The corresponding parameterizations are:

$$\phi_2(N) = 0.732 + 0.172 \left(\frac{2}{N} \right)^{0.6} \quad (12)$$

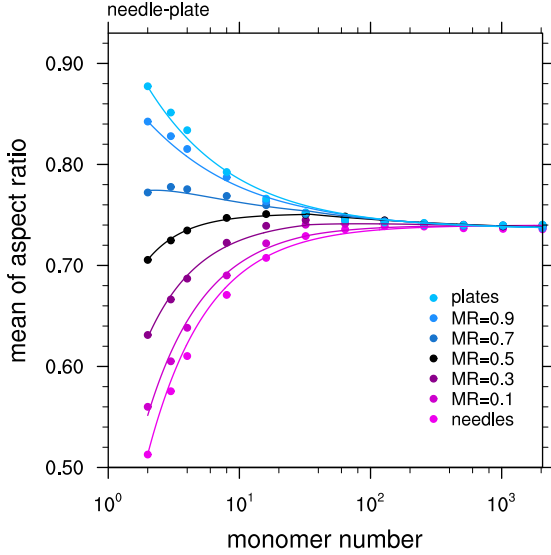
and

$$\phi_{\frac{1}{2}}^{\times}(N) = \begin{cases} 0.756 - 0.0416 \left(\frac{2}{N} \right)^2, & \text{for } N < 16, \\ 0.727 + 0.0271 \left(\frac{16}{N} \right)^{0.3}, & \text{otherwise.} \end{cases} \quad (13)$$

3.3 Cross-sectional area

The cross-sectional area is a key property of hydrometeors, as it influences aerodynamic drag, terminal fall velocity, and the collision kernel (Böhm, 1992a,b,c). Following Böhm's formulation, we define the ellipsoidal area ratio q as the ratio of the snowflake's projected area to that of its circumscribing ellipse.

a) aggregates of needles and plates



b) aggregates of needles and dendrites

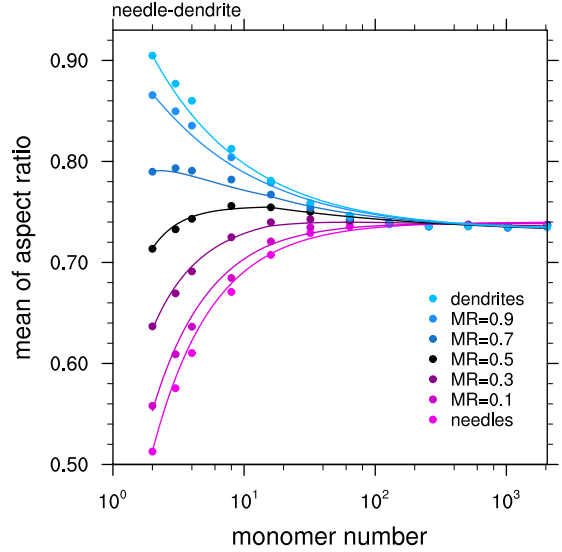


Figure 6: Mean horizontal aspect ratio ϕ_h of aggregates of needles and plates (left) and aggregates of needles and dendrites (right) as a function of monomer number N . Aggregates of mixtures are shown for different monomer ratios MR . Note that the data for pure needle aggregates is the same in both plots. The solid lines are parameterizations using Eqs. (9)–(13), with intermediate values linearly interpolated between $MR = 0$ (needles), $MR = 1$ (plates or dendrites), and $MR = 0.5$.

Figure 7 shows that q decreases with increasing monomer number N . As aggregates grow, they become more fractal and less dense, reducing their area ratios. In contrast to the aspect ratio ϕ , the asymptotic value of q depends on the monomer shape, as the internal structure of the aggregate contributes to the projected area.

For example, aggregates of needles approach an asymptotic value of approximately 0.33, while aggregates of plates approach a level off around 0.41 (Fig. 7a). Because q accounts for internal structure, not just the outer envelope like ϕ , monomer geometry remains influential at all sizes. In other words, each small crystal within the aggregate contributes to the total cross-sectional area, preserving a dependence on monomer shape.

The parameterizations of q_{MR} for aggregates of needles, aggregates of plates and aggregates of the 50/50 mixture are:

$$q_0(N) = 0.327 + 0.386 \left(\frac{2}{N} \right)^{0.75} \quad (14)$$

and

$$q_1(N) = \begin{cases} 0.900 - 0.305 \left(\frac{2}{N} \right)^{1.5}, & \text{for } N < 32, \\ 0.378 + 0.217 \left(\frac{32}{N} \right)^{0.45}, & \text{otherwise.} \end{cases} \quad (15)$$

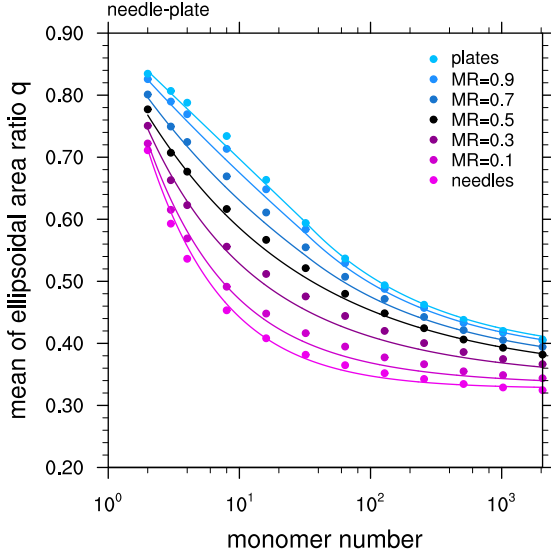
and

$$q_{\frac{1}{2}}(N) = 0.346 + 0.331 \left(\frac{4}{N} \right)^{0.35}. \quad (16)$$

Again, linear interpolation applies for other monomer ratios MR .

Figure 7b confirms that monomer shape influences the area ratio q , as seen in aggregates of dendrites and their mixtures. Aggregates of dendrites have an even lower area ratio q than aggregates of needles, at least for $N < 10$. For intermediate N aggregates of dendrites show a slightly higher q

a) aggregates of needles and plates



b) aggregates of needles and dendrites

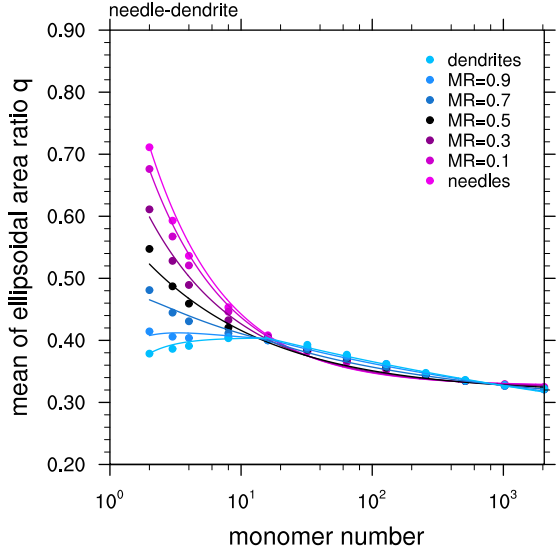


Figure 7: As Figure 6 but for the mean ellipsoidal area ratio q . The solid lines are the parameterizations using Eqs. (14)-(18).

until they converge to a very similar value for large N . The parameterization for the area ratio q of aggregates of dendrites is

$$q_2(N) = \begin{cases} 0.404 - 0.0252 \left(\frac{2}{N}\right)^2, & \text{for } N < 16, \\ 0.178 + 0.2660 \left(\frac{16}{N}\right)^{0.1}, & \text{otherwise.} \end{cases} \quad (17)$$

and for the mixture aggregates of needles and dendrites

$$q_{\frac{1}{2}}^*(N) = 0.315 + 0.173 \left(\frac{3}{N}\right)^{0.45}. \quad (18)$$

These parameterizations of snowflake geometry in terms of D_{\max} , ϕ , and q provide a physically grounded framework for both improving microphysical representations in Lagrangian particle models and enabling more accurate retrievals from remote sensing observations. The required input variables are the mass m , the monomer number N , the monomer ratio MR , and the mass-size relations of plate, needle, and dendrite monomers.

3.4 Joint probability functions

For a stochastic model of snowflake geometry, it is not sufficient to describe individual properties such as D_{\max} , ϕ , and q in isolation; we must also parameterize the correlations between these variables to generate self-consistent and realistic aggregate snowflakes. In particular, a strong correlation exists between the normalized maximum dimension D_{norm} and the aspect ratio ϕ , as illustrated by the snowflake examples in Figs. 3 and 4 and confirmed in Fig. 8, which shows their joint probability density function (PDF).

In the tails of the distributions, values of $\phi > 1$ appear due to the use of the principal axis transform (based on the inertia tensor) and the definition of ϕ via geometric vertical projections. This does not affect the results, as values with $\phi > 1$ are later mapped to $1/\phi$, effectively ensuring that $\phi \leq 1$ and reversing the identity of the two horizontal axes.

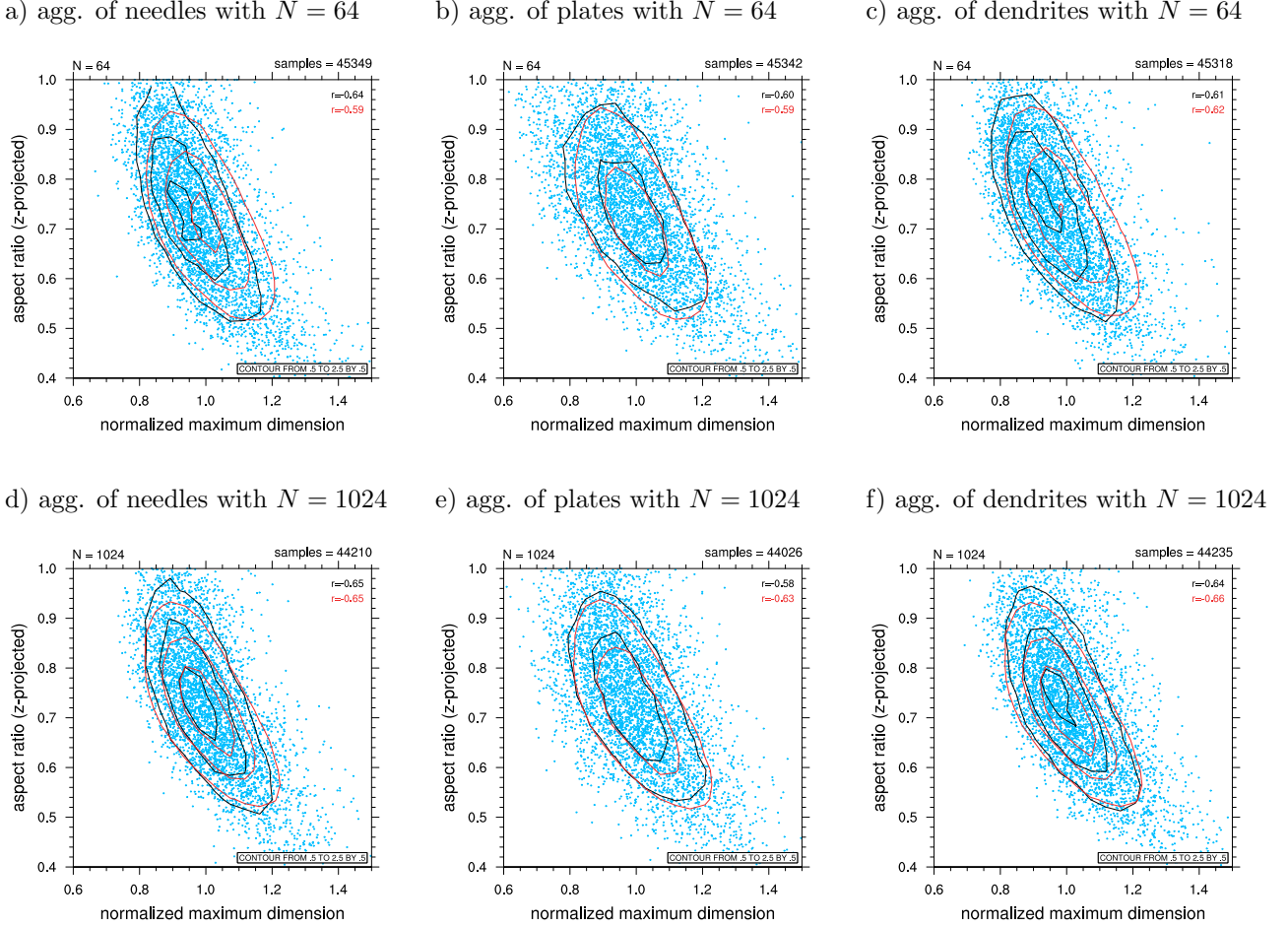


Figure 8: Joint PDF of the normalized maximum dimension D_{norm} and the aspect ratio ϕ for different monomer habits and monomer numbers. The blue dots show thinned-out samples of the dataset, black isolines correspond to the data. The solid red lines are the parameterizations using Eqs. (20)-(23). The correlation coefficient is given in the upper right corner, in black for the data and in red for the parameterization.

The joint PDFs of aggregates of needles exhibits an elongated shape, with correlation coefficients of $r = -0.64$ for $N = 64$ and $r = -0.65$ for $N = 1024$. Aggregates of plates have slightly lower correlation coefficients with of $r = -0.60$ for $N = 64$ and $r = -0.58$ for $N = 1024$. Aggregates of dendrites fall in between with $r = -0.61$ for $N = 64$ and $r = -0.64$ for $N = 1024$.

The joint distribution of ϕ and D_{norm} can be approximated by the product of a lognormal distribution for $P(D_{\text{norm}})$ and a lognormal conditional distribution for $P(\phi | D_{\text{norm}})$:

$$P(\phi, D_{\text{norm}}) = P(D_{\text{norm}}) P(\phi | D_{\text{norm}}). \quad (19)$$

Rather than specifying closed-form expressions for the probability density functions, we define stochastic generation rules suitable for direct implementation in a Monte Carlo framework:

$$P(D_{\text{norm}}) = \exp \left[-\frac{1}{2} \sigma^2 + \mathcal{N}(0, \sigma^2) \right], \quad (20)$$

$$P(\phi | D_{\text{norm}}) = \exp \left[\log (\psi(D_{\text{norm}}) \bar{\phi}(N)) - \frac{1}{2} \sigma_\phi^2 + \mathcal{N}(0, \sigma_\phi^2) \right], \quad (21)$$

where $\mathcal{N}(0, \sigma^2)$ denotes a normally distributed random variable with zero mean and variance σ^2 . This approach allows efficient sampling of aggregate geometries with physically consistent correlations. The

function $\psi(D_{\text{norm}})$ introduces a size-dependent skewness to the conditional distribution:

$$\psi(D_{\text{norm}}) = \begin{cases} 0.55 + 0.45 D_{\text{norm}}^{-3}, & D_{\text{norm}} > 1 \\ 1.45 - 0.45 D_{\text{norm}}^2, & \text{otherwise.} \end{cases} \quad (22)$$

By making the location parameter of the lognormal distribution - the mean in log-space - a function of D_{norm} , the conditional distribution of ϕ (and similarly q below) becomes skewed in a physically meaningful way. For instance, larger aggregates may tend to appear more elongated or irregular in the horizontal plane, a behavior that can be captured by an appropriate choice of the function $\psi(D_{\text{norm}})$. When combined with the parameterization for σ , this results in the joint PDF shown by the red isolines in Fig. 8, yielding correlation coefficients of $r = -0.60$ for $N = 64$ and $r = -0.65$ for $N = 1024$ for aggregates of needles; $r = -0.60$ for $N = 64$ and $r = -0.64$ for $N = 1024$ for aggregates of plates; and $r = -0.63$ for $N = 64$ and $r = -0.65$ for $N = 1024$ for aggregates of dendrites. Given the uncertainties of the aggregation model, the accuracy of these parameterizations should be sufficient. Interestingly, the functional form of ψ is independent from the monomer habit and the same relation can be used for all aggregates. The standard deviation is given by

$$\sigma_\phi = 0.12 + \frac{0.2}{\sqrt{N}} \quad (23)$$

independent from monomer habit.

For the joint probability of D_{norm} and the ellipsoidal area ratio q we use the same ansatz with a lognormal for the conditional distribution

$$P(q | D_{\text{norm}}) = \exp \left[\log \left(\chi_{MR}(D_{\text{norm}}) \bar{q}(N) \right) - \frac{1}{2} \sigma_q^2 + \mathcal{N}(0, \sigma_q^2) \right], \quad (24)$$

with $\sigma_{q,0} = 2.07$, $\sigma_{q,1} = 0.127$, $\sigma_{q,2} = 0.180$, $\sigma_{q,\frac{1}{2}}^\circ = 0.144$ for the 50/50 mixture of needles and plates, and $\sigma_{q,\frac{1}{2}}^\circ = 0.168$ for the 50/50 mixture of needles and dendrites.

For aggregates of needles $\chi_0(D_{\text{norm}})$ is given by:

$$\chi_0(D_{\text{norm}}) = \begin{cases} 0.70 + 0.20 D_{\text{norm}}^{-2} & D_{\text{norm}} > 1 \\ 1.25 - 0.35 D_{\text{norm}}^3 & \text{otherwise.} \end{cases} \quad (25)$$

and for all other cases, plates, dendrites, and both types for mixture, the following approximation applies:

$$\chi_1(D_{\text{norm}}) = \chi_2(D_{\text{norm}}) = \chi_{\frac{1}{2}}(D_{\text{norm}}) = \begin{cases} 0.75 + 0.20 D_{\text{norm}}^{-2} & D_{\text{norm}} > 1 \\ 1.40 - 0.45 D_{\text{norm}}^3 & \text{otherwise.} \end{cases} \quad (26)$$

The joint probability density functions (PDFs) of D_{norm} and q for pure aggregates of needles, plates and dendrites are shown in Fig. 9. For aggregates of plates, the correlation between q and D_{norm} is moderately strong. The aggregate dataset yields correlation coefficients of $r = -0.49$ for $N = 64$ and $r = -0.55$ for $N = 1024$ (Figs. 9b,e). The parameterization performs reasonable, but with slightly higher correlation of $r = -0.57$ for both N . Aggregates of needles exhibit a weaker relationship. In the data, the correlation drops to $r = -0.46$ for $N = 64$ and $r = -0.29$ for $N = 1024$ (Figs. 9a,d). The parameterization captures this trend, yielding $r = -0.35$ for both values of N . Especially for the case of aggregates of needles with $N = 64$ (Fig. 9c) the strong skewness in q observed for $D_{\text{norm}} < 1$ is not fully captured by the simple ansatz for the joint PDF. Consequently, the parameterization underestimates the probability of needle aggregates with a high q in the tail of the distribution. Aggregates of dendrites are somewhat in between and show a significant but weaker nonlinear tail.

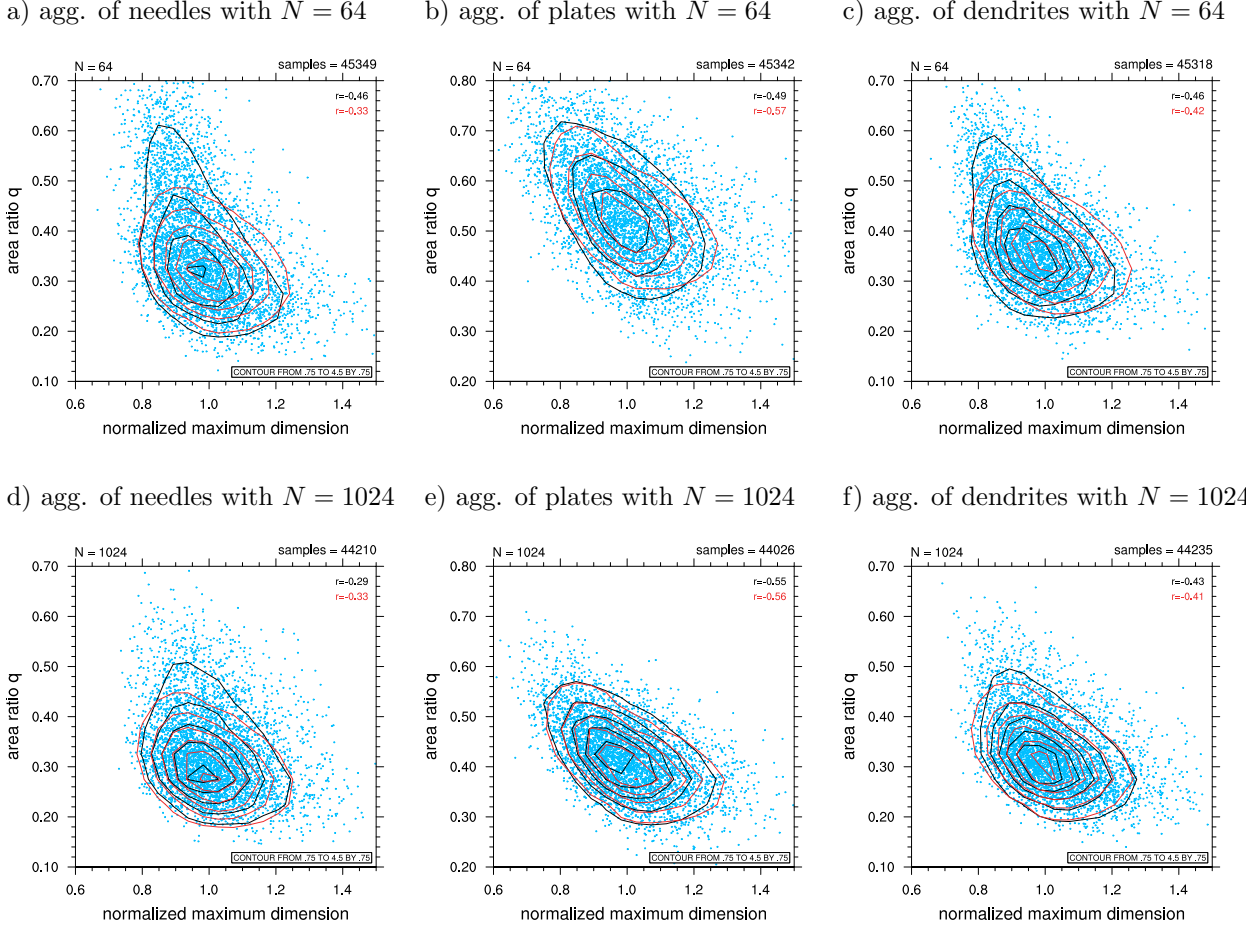


Figure 9: As Fig. 9, but for the joint correlation of the normalized maximum dimension D_{\max} and the ellipsoidal area ratio q . The solid red lines are the parameterizations using Eqs. (24)-(26).

Aggregates of mixtures tend to resemble their more oblate component in terms of q ; corresponding figures are omitted for brevity.

While our simple joint PDF model captures general trends and the essential behavior, it is not able to describe the full complexity of aggregate snowflakes in a quantitative form. For small N , and especially for $N < 10$, the variability in q as reflected in the joint PDF is higher and more strongly influenced by individual monomer geometry. This complexity for small N may warrant a more detailed treatment in future work.

4 Application in McSnow

4.1 Implementation

The Monte Carlo Lagrangian Particle Model *McSnow* predicts eight key properties of hydrometeors. These properties include the ice mass m , the monomer number N of aggregates, the rime mass m_r , the rime volume V_r , the liquid mass m_ℓ , and the frozen mass m_f . In addition, when predicting the habit of primary crystals (or monomers), the model introduces the prognostic variables of the monomer aspect ratio ϕ_m and the ice volume V_i (Welss et al., 2024), with the latter being essential for characterizing branching and hollowing of crystals. Furthermore, the multiplicity ξ is used to describe the number of real particles represented by a super-particle (Shima et al., 2009).

While the maximum dimension and other geometric properties, such as the ellipsoidal area ratio q , are not prognostic variables in *McSnow* at present, they can be diagnosed from the eight prognostic variables, combined with assumptions about particle shape. For instance, Seifert et al. (2019) discuss geometry assumptions for partially rimed snowflakes and graupel. In this work, we extend the framework to include stochastic aggregates with habit information, leveraging the joint PDFs and geometric relationships discussed in the previous section. The maximum dimension D_{\max} for aggregate snowflakes will be treated as a stochastic pseudo-prognostic variable, as explained in the following.

The stochastic aggregate snowflake framework described earlier is now integrated into *McSnow*. In addition to the monomer number N , we introduce a monomer count for prolate crystals, N_p , which simply counts the monomers in an aggregate with $\phi_m > 1$. Using this, the monomer ratio MR for an individual aggregate is calculated as:

$$MR = \frac{N_p}{N} \quad (27)$$

At first glance, using the monomer ratio MR of an individual aggregate may appear inconsistent with Section 3, where MR is derived from the size distribution of primary crystals. However, in the context of a super-particle, MR naturally represents an ensemble average over the ξ real particles it stands for, thereby resolving the apparent inconsistency.

In addition, the number of dendrite monomers in each aggregate is tracked using the counter N_d . Dendrite monomers are defined as oblate monomers with an ellipsoidal area fraction q smaller than 0.5 at the time of collision. Given N , N_p , and N_d , the number of plate monomers in an aggregate is $N_o = N - N_p - N_d$. If $N_d > N_o$, the aggregate is treated as a mixture of needles and dendrites; otherwise, as a mixture of needles and plates. This simplification avoids complicated multidimensional interpolation in a three-component mixture and neglects the existence of plate–dendrite combinations. This approach can be generalized if observations show that such mixtures are more relevant than currently assumed.

After a successful collision event between ice crystals and/or aggregate snowflakes, the geometry of the resulting new aggregate has to be determined. Given the mass m , the monomer number N , and the monomer ratio MR of the new aggregate, the mean monomer size \bar{D}_{mono} is computed using Eq. (1). For aggregates of mixtures the geometry coefficients of the monomers are interpolated with:

$$a_{MR} = \exp(MR \log(a_1) + (1 - MR) \log(a_0)) \quad (28)$$

$$b_{MR} = MR b_1 + (1 - MR) b_0. \quad (29)$$

The normalized maximum dimension for the new aggregate is then sampled from the following log-normal distribution:

$$D_{\text{norm}} \sim \exp\left[-\frac{\sigma^2}{2} + \mathcal{N}(0, \sigma^2)\right], \quad (30)$$

where \sim denotes that a random variate is drawn from the distribution specified on the right-hand side. The maximum dimension D_{\max} is then computed by inverting Eq. (3), yielding:

$$D_{\max} = D_{\text{norm}} \bar{D}_{\text{mono}} \left(\frac{N}{N_0}\right)^{\eta} + D_{\min}. \quad (31)$$

Remember that D_{norm} is dimensionless, which ensures the dimensional consistency of this equation. Once D_{norm} is sampled, corresponding random variates for the aspect ratio ϕ and the area ratio q are drawn from the following distributions:

$$\phi \sim \exp\left[\log(\psi(D_{\text{norm}}) \bar{\phi}(N)) - \frac{1}{2}\sigma_{\phi}^2 + \mathcal{N}(0, \sigma_{\phi}^2)\right], \quad (32)$$

and

$$q \sim \exp \left[\log (\chi_{MR}(D_{\text{norm}}) \bar{q}(N)) - \frac{1}{2} \sigma_q^2 + \mathcal{N}(0, \sigma_q^2) \right]. \quad (33)$$

With the geometric properties D_{\max} , ϕ , and q available, the terminal fall velocity and collision efficiency of the newly formed aggregate can be calculated using Böhm's parameterizations (Böhm, 1992a,b,c), as described and concisely summarized in Appendix A of Welss et al. (2024). These parameters, together with the underlying geometric assumptions, provide the basis for computing the collision kernel in subsequent aggregation or riming events, ensuring consistent microphysical treatment. The random variates for D_{\max} , ϕ , and q assigned to each Monte Carlo aggregate are stored and continuously updated to reflect changes caused by microphysical processes other than collision. For depositional growth, for example, the update of D_{\max} is calculated as

$$D_{\max}^{\text{new}} = D_{\max}^{\text{old}} \left(\frac{m + \Delta m_{\text{depo}}}{m} \right)^\zeta \quad (34)$$

where Δm_{depo} is the mass gain from deposition in the current time step, and ζ is defined as

$$\zeta = \frac{1}{N} \left(\frac{1}{b_h} + \frac{N-1}{b_{\text{agg}}} \right). \quad (35)$$

and b_h is again the interpolated monomer geometry exponent and $b_{\text{agg}} = 2.1$. This ansatz accounts for the geometric influence of monomers at low N via the exponent β_i , while ensuring that ζ asymptotically approaches $1/b_{\text{agg}}$ for large aggregates.

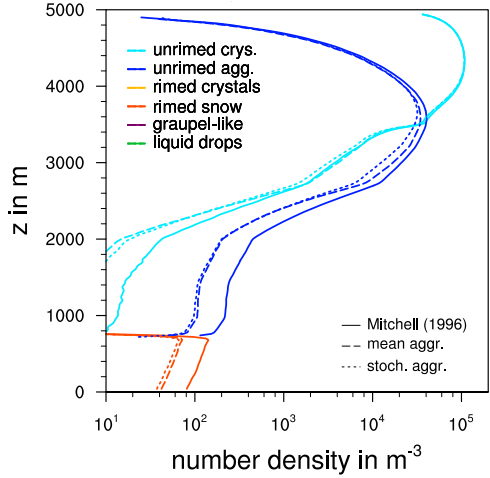
During depositional growth, ϕ and q are held constant. While this lacks direct physical validation, it provides a practical and robust approximation given the scarcity of detailed observational or simulation data. Importantly, it aligns with observations indicating that the mass-size relation for snowflake aggregates typically follows a consistent scaling law, $m \propto D_{\max}^p$ with $p \approx 2$, even in the presence of depositional growth (Locatelli and Hobbs, 1974; Mitchell et al., 1990; Leinonen et al., 2021).

A key limitation of the approach presented here is the absence of aggregate memory throughout collision events: a new random geometry is generated for each collision event, with no retention of structural features from the parent particles. In nature, aggregates likely preserve aspects of their precursors, such as shape asymmetries or alignment. Incorporating such memory effects, however, would significantly complicate the stochastic scheme, as the joint probability distributions introduced in the previous section would need to account for the properties of both parent particles resulting in high-dimensional PDFs. For a Monte Carlo Lagrangian particle model, in which each super-particle represents an ensemble of real particles, the neglect of parent-specific memory appears to be a reasonable and pragmatic simplification. Nonetheless, since *McSnow* explicitly tracks the individual properties of parent particles, this information could, in principle, be used to inform the geometry of the resulting aggregate in a more physically consistent way.

4.2 Idealized 1D simulations

To understand the impact of the stochastic geometry of aggregate snowflakes on the microstructure of clouds, we perform one-dimensional simulations using a stationary atmospheric profile similar to that in Welss et al. (2024), Section 5. The temperature profile is defined by a surface temperature of 273 K and a constant lapse rate of 0.0062 K m^{-1} , within a domain extending up to 5000 m (case 1) and 4000 m (case 2). Water vapor, liquid water, and temperature are prescribed and held constant; no microphysical processes modify them during the simulation. Particles nucleate randomly within the uppermost 1500 m of the domain and grow by vapor deposition at a constant supersaturation with respect to ice of 5%. Below 1000 m altitude, they pass through a cloud layer with a liquid water

a) number density



b) mass density

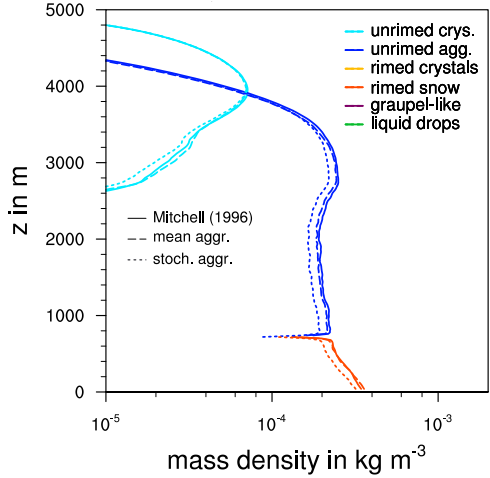


Figure 10: Vertical profiles of number and mass densities for the quasi-stationary state of 1D McSnow simulations (case 1). Super-particles are categorized as unrimed crystals, unrimed aggregates, rimed crystals, rimed aggregates, and liquid drops. The control simulation uses empirical aggregate geometry based on M96 (solid lines). The simulation using the new stochastically generated aggregates is represented by dotted lines. Dashed lines correspond to a simulation with the new aggregates, but using zero standard deviations, i.e., the deterministic mean snowflakes.

mixing ratio of 0.1 g/kg, leading to riming similar to a seeder–feeder cloud. The initial multiplicity is 16×10^4 , and the vertical grid spacing of the Eulerian grid is 250 m. These settings result in more than 2000 super-particles per grid box throughout the column.

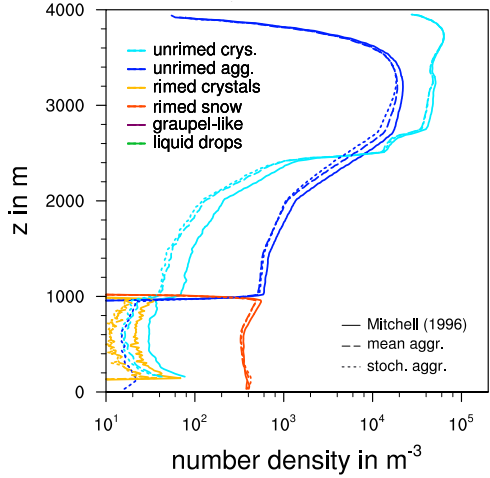
For each case, we compare three simulations: one using the empirical aggregates from Mitchell (1996, M96 hereafter), one using the stochastically generated aggregates described in the previous section, and one using the deterministic mean of the new aggregates. In the deterministic mean snowflake experiment, all stochastic variability is removed by setting standard deviations to zero, such that each snowflake of a given mass and monomer number has identical properties.

Figure 10 shows vertical profiles of particle number and mass density, averaged over the final 3 hours of a 6-hour simulation. The uppermost region of the domain is dominated by primary ice crystals growing via vapor deposition. Aggregation rapidly becomes significant, and by 4000 m, aggregate snowflakes dominate the mass density. Despite this, primary crystals continue to nucleate and thus remain dominant in number density above 3500 m. Below 3500 m, where no nucleation occurs, aggregate snowflakes efficiently deplete primary ice crystals, leading to a notable drop in their concentration. Only a few primary particles survive and escape collection by aggregates. While the mass density of aggregates remains fairly constant between 3000 m and 1000 m height, the number density decreases due to aggregation. Below 1000 m, riming increases the mass density of aggregate snowflakes, which become at least partially rimed.

The three simulations yield similar results, as these 1D simulations are strongly constrained by the assumed atmospheric profile. In number density, the largest difference occurs between the M96 aggregates and the mean aggregates. In mass density, the stochastic aggregates lead to significantly lower values below 3500 m height. These differences emerge in the size and terminal fall velocity of the aggregates, which in turn influence both mass and number densities.

The fact that number and mass densities of aggregate snowflakes are slightly reduced when using stochastic sampling suggests that aggregation between aggregates is enhanced due to increased variability among the particles. This additional aggregation increases the average size and terminal

a) number density



b) mass density

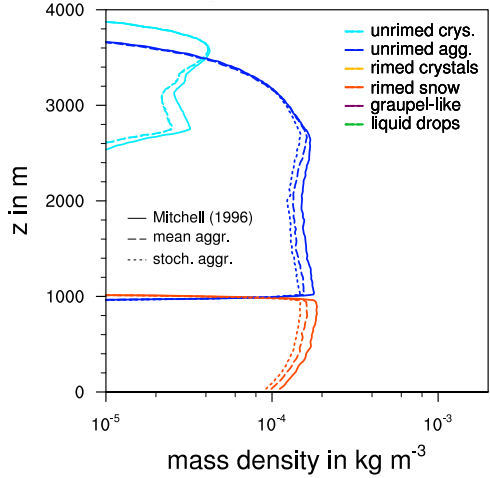


Figure 11: As in Figure 10, but for case 2 with a domain top at 4000 m and a nucleation layer in the uppermost 1500 m.

velocity of the snowflakes, which in turn lowers the mass density. A second effect is that more compact aggregates with $D_{\text{norm}} < 1$ have higher terminal fall velocities, and this is not fully compensated by the slower fall speeds of elongated aggregates. Hence, on average, stochastic sampling increases terminal fall velocity and, consequently, reduces mass density. This nonlinearity of the terminal fall velocity — whereby the mean fall speed of a particle ensemble exceeds the fall speed of the mean geometry — results in an increase in the bulk terminal fall velocity of approximately 5 %. This behavior arises from the same mechanism described by Dunnavan (2021), where variability in snowflake shape leads to enhanced ensemble-mean fall speeds. While Dunnavan reported increases of up to 60 % in fall speeds of individual particles, our smaller value represents the average effect over a broader particle population.

Overall, the sensitivity to the variability of snowflake geometry, as represented by the stochastic sampling approach, is weaker than expected. This indicates that polydispersity arising from variation in aggregate mass and monomer number dominates the aggregation process, while random variability in maximum dimension among aggregates with the same mass and monomer number has only a second-order effect on the collision rate.

This is confirmed by case 2, with a domain top at 4000 m. For this case, which is dominated by dendrites as we will see later, the main difference in mass density is between M96 and the mean aggregates. The effect of stochastic sampling is even smaller than in case 1. An interesting difference between case 1 and case 2 is that the mass density increases in the riming layer for case 1 but decreases for case 2. This shows that, depending on the microstructure of snowflakes, either the mass increase due to riming can dominate (as in case 1), or the dilution effect due to the increase in terminal fall velocity (as in case 2).

To delve deeper into the simulated microstructure of snowflakes and the differences between case 1 and case 2, Figures 12 and 13 show scatter plots of various ice particle properties as a function of maximum dimension. Both simulation with stochastic aggregates use the prognostic approach to aggregate habit described earlier. For the mass-size relation, the mean aggregates behave similar to the empirical power law of M96. Using stochastic sampling yields a variability resembling Figure 1 by construction.

M96 does not provide an aspect ratio for aggregates, so in McSnow we assume $\phi = 1$ for M96 aggregates. The new aggregates are slightly prolate with $\phi = \phi_h^{-1} \approx 1.3$ in the deterministic mean

Mitchell (1996)

b) mean aggregates

c) stochastic aggregates

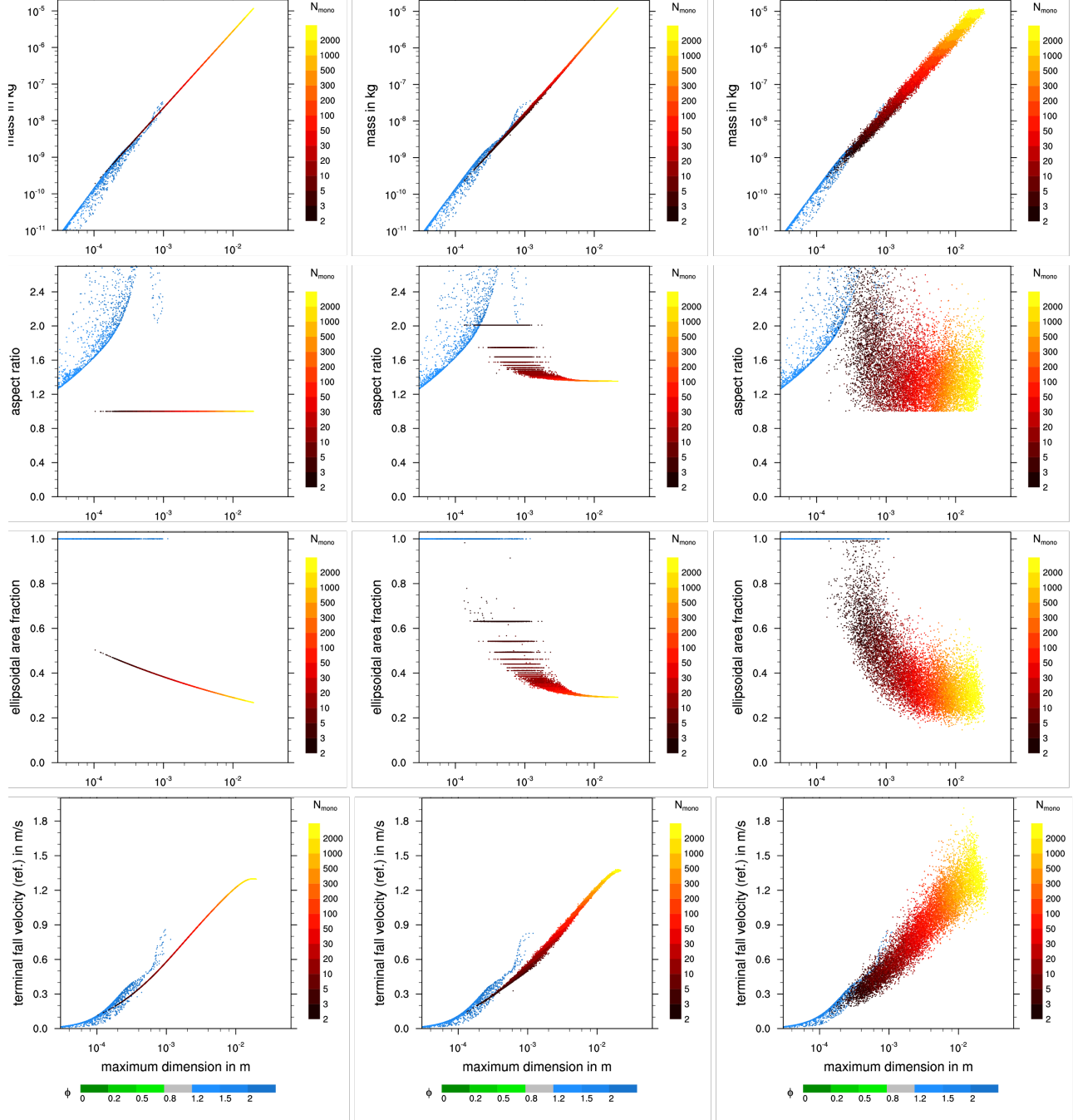


Figure 12: Scatter plots of the m – D , ϕ – D , q – D , and v – D relations for case 1 using empirical aggregates from M96 (left), mean aggregates (middle), and stochastic aggregates (right). All plots share the same x -axis showing the maximum dimension D . Color bars represent aspect ratio ϕ of monomers (green–grey–blue), aggregates are colored by monomer number N (brown–red–yellow). Fall velocities are adjusted to reference conditions $p = 1000$ hPa and $T = 273.15$ K.

Mitchell (1996)

b) mean aggregates

c) stochastic aggregates

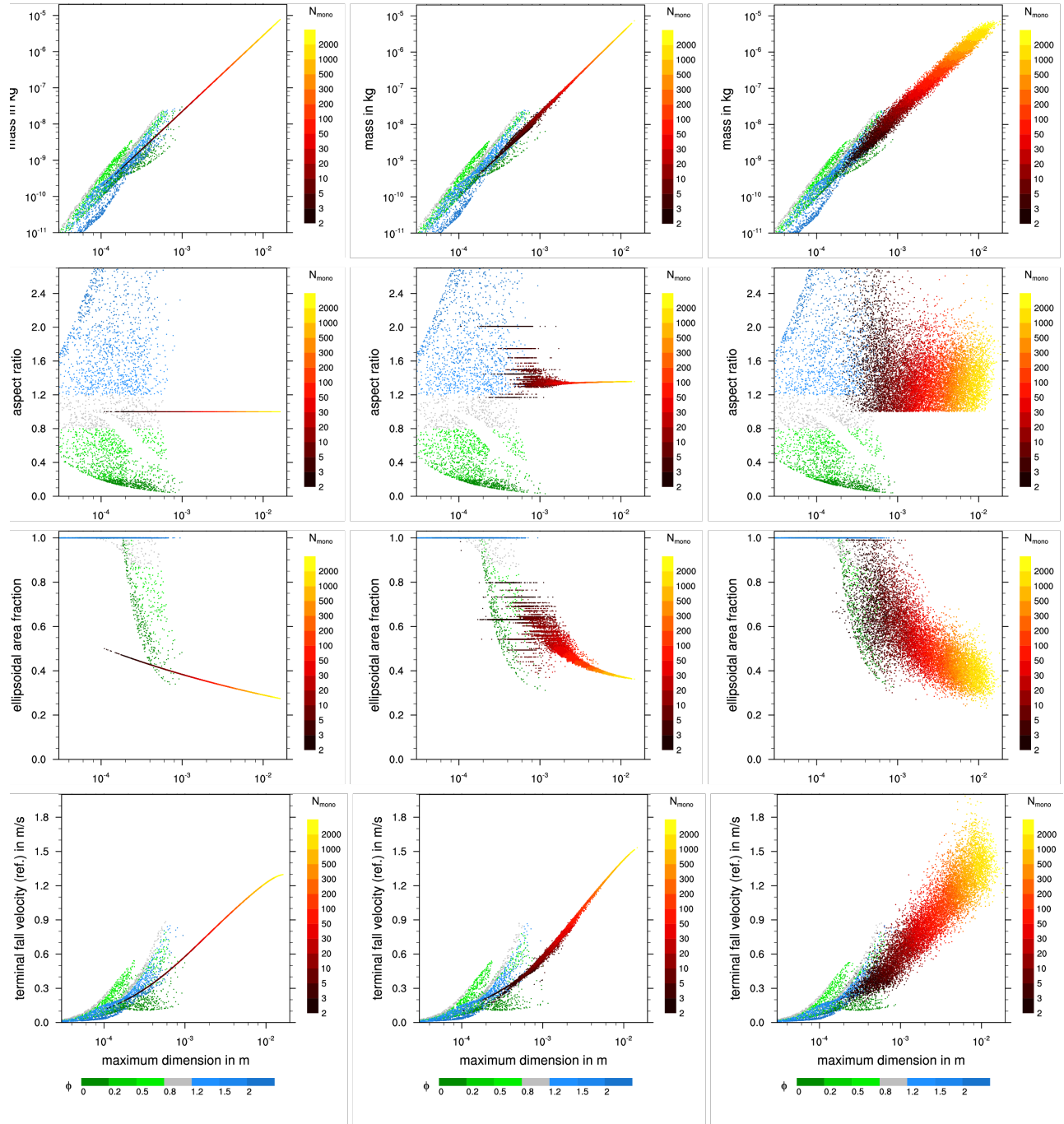
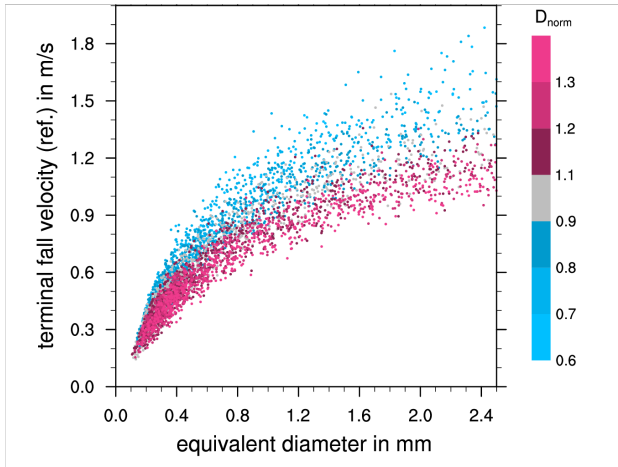


Figure 13: As in Figure 12, but for case 2 with a domain top at 4000 m and a nucleation layer in the uppermost 1500 m.

a) case 1



b) case 2

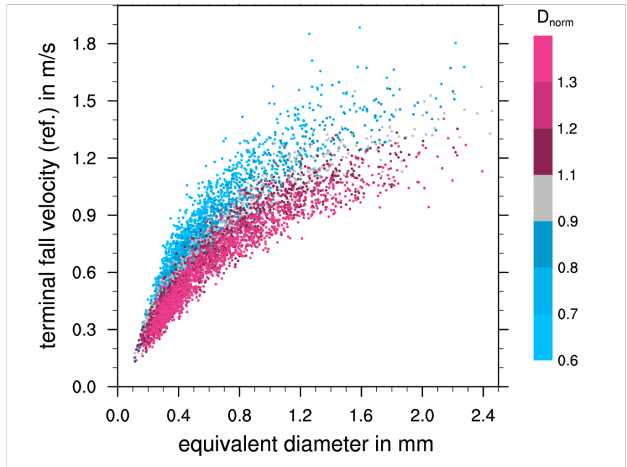


Figure 14: Scatter plot of terminal fall velocity of aggregate snowflakes as a function of equivalent diameter for case 1 (left) and case 2 (right). Colors indicate the normalized maximum dimension D_{norm} , with $D_{\text{norm}} > 1$ for elongated aggregates and $D_{\text{norm}} < 1$ for compact aggregates. Velocities are adjusted to 1000 hPa and 273.15 K.

(see Figure 6). The ellipsoidal area ratio q decreases with size. M96 and our new deterministic aggregates behave similarly. That M96 has a lower q for small aggregates partly results from our assumption of $\phi = 1$. Horizontal lines for mean aggregates in Figure 12b reflect that ϕ and q are functions of monomer number N only. Case 1 is dominated by needle monomers, shown as blue markers for primary crystals. Case 2 shows a wider range of habits from prolate to oblate, yielding slightly larger variability in aggregate properties.

The stochastic variability is especially large for aspect ratio ϕ and area fraction q . The new aggregates produce fall velocities similar to M96, with realistic spread, consistent with in-situ observations. This variability results directly from differences in ϕ and q . For primary crystals, prolate particles fall significantly faster than oblate ones of the same mass. Plotting terminal fall velocity as function of maximum dimension gives a more complicated behaviour and oblate particles can indeed fall faster than prolate crystals of the same size. Large aggregate snowflakes show terminal velocities up to 1.5 m/s in the mean aggregate case, rising to 1.8 m/s with stochastic variability. For case 2, the terminal fall velocity of the new aggregate snowflakes with $D_{\text{max}} > 1$ mm is significantly higher than with M96 aggregates for this case. Figure 14 confirms that compact aggregates ($D_{\text{norm}} < 1$) fall faster than elongated ones ($D_{\text{norm}} > 1$).

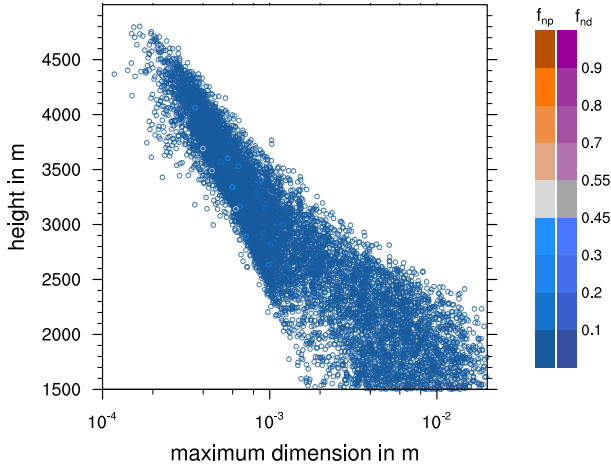
Figure 15 shows the dominant habits in the simulated aggregates. Case 1 is consistently dominated by aggregates of needles at all altitudes. In case 2, aggregates of needles dominate above 3000 m, with a transition to plate- and dendrite-dominated aggregates below. Near the surface a rich mix of aggregate habits is found with large aggregates dominated by dendrites. Validating these predictions with modern video disdrometers requires a more realistic model setup and is left for future work.

5 Simulating radar signatures of stochastic aggregates

5.1 A radar forward modeling framework for McSnow

Forward models, especially in the microwave region, are key components for atmospheric model evaluation and data assimilation. For these forward models, the optical properties of particles simulated

a) case 1



b) case 2

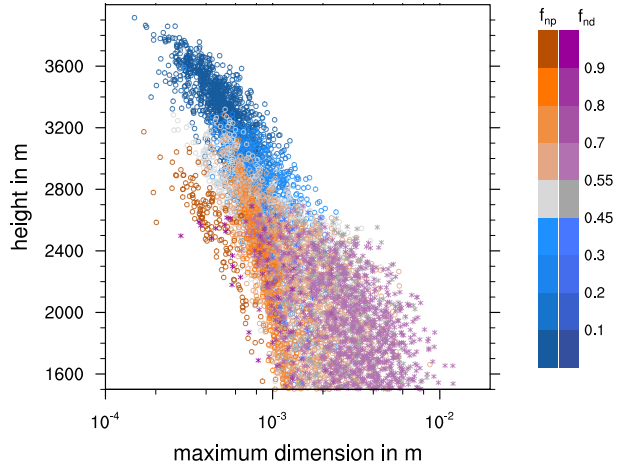


Figure 15: Scatter plot of aggregate snowflake size versus height. Colors indicate the number ratio of the binary habit mixture, with the dominant monomer habit shown as follows: blue for needles, orange for plates, and magenta for dendrites. Marker shapes denote mixed habit types: circles for needle-plate aggregates and stars for needle-dendrite aggregates. Data points have been thinned for clarity.

in the atmospheric model need to be known. To this end, the discrete-dipole approximation (DDA; Draine and Flatau (1994)) is often employed, as it provides an accurate approximation of the scattering properties of individual particles with arbitrary shapes. In von Terzi et al. (2025), a database containing the scattering properties of 3,077 individual ice crystals was developed, which is particularly suitable for the model output of McSnow. For the present study, this database was extended to include 7,010,688 aggregates. The three-dimensional representations of these aggregates were generated as described in Section 2.

The Amsterdam DDA (ADDA; Yurkin and Hoekstra (2007, 2011)) code is used to calculate the optical properties of these particles at common cloud and precipitation radar frequencies, including 5.6, 9.6, 35.6, and 94 GHz. All particles are assumed to be aligned with their largest axis horizontally. For each particle, only a single radar viewing angle is simulated, so that at all frequencies for a given particle at one elevation and one azimuth angle are computed. This approach differs from most previous studies, where each individual particle is typically simulated at multiple orientations (e.g. Lu et al., 2016; Brath et al., 2020; von Terzi et al., 2025). For example, in von Terzi et al. (2025), each particle is simulated at 37 elevations and 16 azimuth orientations. Such an approach is often chosen to reduce the number of distinct particles that need to be generated, as especially for aggregates, the scattering properties can vary significantly with viewing angle.

In contrast, our study leverages the large aggregate database to provide substantial variability in scattering properties even when only one radar viewing angle per particle is considered. In total, we calculated scattering properties for 7,010,688 particles. For comparison, von Terzi et al. (2025) included 3,077 ice crystals simulated at 37 elevations and 16 azimuth orientations, corresponding to 1,821,584 individual calculations, approximately four times fewer than the number of aggregates used here. The major advantage of calculating the scattering properties for such a large number of particles is the wide variability in physical properties (e.g., D_{\max} , mass, aspect ratio) that can be simulated. While the total number of scattering calculations in our study is only about four times larger than that of the crystals used in von Terzi et al. (2025), the total number of different physical properties covered is approximately 2,300 times larger. This makes it particularly suitable for models with widely

varying physical properties, such as the stochastic aggregates introduced here.

For each particle, the amplitude and Mueller matrix entries at 0° and 180° scattering directions are calculated. From these matrix entries, the single-particle reflectivity at horizontal (Ze_H) and vertical (Ze_V) polarizations, the extinction cross sections at horizontal ($c_{ext,h}$) and vertical ($c_{ext,v}$) polarizations, as well as the specific differential phase shift KDP, are derived using well-known equations (e.g., von Terzi et al., 2025). These values are stored in a lookup table (LUT), which is then interfaced to the forward operator McRadar as described in detail in von Terzi et al. (2025).

In von Terzi et al. (2025), the focus was on super-particles, where an azimuthal average of the scattering properties was calculated for each particle. These azimuthally averaged scattering properties were then assigned uniformly to each super-particle. This means that all the real particles represented by a single super-particle shared the same averaged scattering properties, simplifying the calculation but potentially smoothing out orientation variability.

In contrast, our new implementation operates at the level of real particles represented by each super-particle and samples the scattering properties based on a single radar viewing angle per particle (so one elevation and one azimuth angle are sampled per particle), assuming the particles fall with their largest dimension oriented horizontally. Since only one radar viewing angle is considered for each real particle, azimuthal averaging of scattering properties cannot be performed as before. Instead, the best-fitting scattering properties of individual particles are assigned to each simulated real particle, allowing for slight variations in scattering properties among the real particles associated with each super-particle.

This approach is analogous to the previous averaging method in the following way: if a super-particle has a multiplicity of 16, matching the number of azimuth directions used in von Terzi et al. (2025), one could theoretically assign the scattering properties from each azimuth angle to a corresponding real particle within that super-particle. The total reflectivity (Ze) would then be obtained by summing the contributions from all real particles. Alternatively, the older approach averaged over all azimuth angles first and assigned this average to the entire super-particle, then multiplied by the multiplicity to obtain the total reflectivity. Both methods yield equivalent results in principle.

Although in our case the multiplicity does not typically equal the number of azimuth directions probed, the very large number of particles considered ensures that the overall statistical behavior of the scattering properties remains comparable.

The LUT contains information on particle mass, size, habit, and elevation, while McSnow provides mass, size, habit, and the desired radar setup provides the radar elevation. The goal is to retrieve particles whose mass, size, habit, and elevation correspond to those in the LUT. Here, *habit* refers to the types of monomers in the aggregate (i.e., needles, dendrites, and plates) and their ratios (see Section 4 for more details). The selection is performed using a K-Dimensional Tree (K-D Tree), where for each super-particle, candidates from the lookup table are identified based on target mass, size, habit, and elevation. A variability of 5% in mass and D_{max} , 50% in monomer ratio, and 5° in elevation is allowed. The variability in elevation allows for a flexible treatment of the particle canting angle, simulating wobbling effects due to, e.g., turbulence in the overall fall behavior of the particles. Out of all candidates, $N = \min(n_{cand}, \xi)$ are randomly selected, where n_{cand} is the number of found candidates and ξ is the multiplicity of the super-particle. These are weighted by $wgt = \xi/n_{cand}$, ensuring that $N \cdot wgt = \xi$. This weighing needs to be done, as for super-particles with large ξ and small variabilities in mass, D_{max} and monomer ratio, not enough candidates can be found to select one candidate for each real particle. The scattering properties of the super-particle are then obtained as the weighted sums of the scattering properties of all selected candidates.

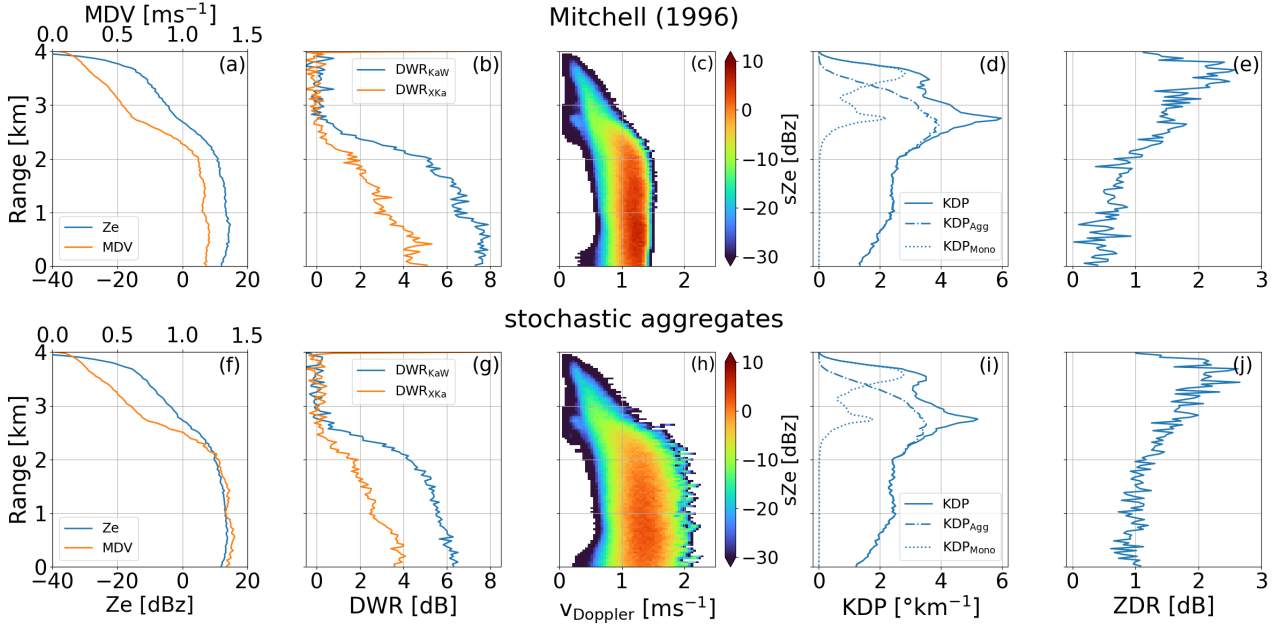


Figure 16: Radar forward simulations of case 2 using empirical aggregates from M96 (first row) and stochastic aggregates (second row). The first column (panels (a) and (f)) shows the radar reflectivity (Ze) and mean Doppler velocity (MDV) at Ka-band (35.6 GHz) and 90° elevation (zenith view). The second column (panels (b) and (g)) shows the reflectivity differences (in dB, commonly denoted as dual-wavelength ratio) at zenith between Ka- and W-band (94 GHz) and X (9.6 GHz) and Ka-Band. The third column (panels (c) and (h)) shows the zenith spectral reflectivity (sZe) at Ka-Band, the fourth column (panels (d) and (i)) shows the specific differential phase shift KDP at W-Band and 30° elevation, as well as the contributions of aggregates and monomers to the total KDP. The fifth column (panels (e) and (j)) shows the differential reflectivity ZDR at 30° elevation and W-Band.

5.2 Simulated radar signatures of case 2

To compare the radar signatures of the M96 aggregates and the stochastic aggregates, case 2 was forward simulated at 9.6 (X-band), 35.6 (Ka-band), and 94 (W-band) GHz, and at 30° and 90° elevation. Figure 16 shows the main radar moments: radar reflectivity factor (Ze), mean Doppler velocity (MDV), the dual-wavelength ratios (reflectivity difference in dB) between Ka- and W-Band DWR_{KaW} and between X- and Ka-Band DWR_{XKa} , the polarimetric variables specific differential phase shift (KDP) and differential reflectivity (ZDR), as well as the spectral reflectivity (sZe). Positive Doppler velocities indicate motions towards the radar.

The case study displays typical features often observed in ice cloud measurements (von Terzi et al., 2022, and references therein). Aggregation increases both Ze and DWR, at Ka- and W-band as well as at X- and Ka-band, especially towards the ground. The strongest increase in DWR occurs at temperatures between -20°C and -10°C , corresponding to the dendritic growth layer (DGL), which is known for high aggregation efficiencies Connolly et al. (2012). In the same region, the Doppler spectra show increasing sZe, consistent with particle growth. Interestingly, at 2.75 km (-17°C), a secondary, slowly falling mode appears in the spectrum. This new mode arises from freshly formed, small, plate-like ice crystals at that temperature. Although aggregation acts as a sink for such crystals, collision efficiency is strongly size-dependent; the smallest crystals have the lowest chance of colliding with aggregates. As a result, a distinct mode of small ice crystals develops. Closer to the ground, these crystals grow and fall faster, while no new crystals are produced. Consequently, the secondary

mode merges with the main one and becomes indistinguishable, even though small crystals remain present down to near-surface levels.

KDP shows a pronounced peak at 2.75 km, coinciding with the appearance of the secondary Doppler spectra mode. KDP typically reflects increases in particle size and concentration, and here it indicates large numbers and sizes of ice particles at this height. The peak is caused by both aggregates and monomers, though aggregates dominate the signal. As aggregation continues, the total number concentration decreases, and KDP correspondingly declines towards the ground.

ZDR, in contrast, peaks at 3.5 km, slightly higher than the main KDP maximum. The peak in ZDR coincides with the largest KDP of monomers. However, towards the ground, aggregates dominate KDP in this case, off-setting the main KDP peak and the ZDR peak. This vertical separation of ZDR and KDP has been reported in many earlier studies (e.g. von Terzi et al., 2022; Moisseev et al., 2015), although the underlying cause remains debated.

When comparing the two experiments, the overall radar signatures appear similar, but important differences emerge. The most evident difference is seen in the Doppler spectra: it is much broader for the stochastic aggregates, reflecting the large variability in their physical properties, especially in terminal fall velocity (cf. Fig. 13). The fast-falling edge extends to 2 m s^{-1} for the stochastic aggregates, compared to 1.5 m s^{-1} for the M96 aggregates. Consequently, MDV is larger in the stochastic case (1.4 m s^{-1} versus 1.2 m s^{-1}). Cloud radar observations in mid-latitude frontal clouds commonly show a Doppler spectrum width around 2 m/s above the melting layer (see e.g. Figs. 3 and 5 of von Terzi et al. (2022)) similar to the *McSnow* simulation with stochastic aggregates.

The mean aggregate size is similar between the two experiments. Surprisingly, DWR_{KaW} is smaller for the stochastic aggregates (a maximum of 6.1 dB in contrast to 7.7 dB), while DWR_{XKa} remains the same. For a single particle type (e.g. dendritic aggregates with a uniform structure), a smaller DWR usually implies smaller aggregate size. However, the internal mass distribution also matters: denser particles can yield larger DWR_{KaW} but similar DWR_{XKa} compared to less dense ones (Mason et al., 2019; Kneifel et al., 2015). Here, the habit of the aggregates and therefore their internal structure is of course different between the two experiments, the smaller DWR_{KaW} might indicate that the stochastic aggregates are less dense. However, in addition, the aggregate size distribution itself affects the relationships between DWR_{XKa} and DWR_{KaW} (Mason et al., 2019). Looking at the size distributions for this case study, it becomes evident that the size distribution of the stochastic aggregates is wider, encompassing larger and smaller particles than the M96 experiment. Therefore, a combination of internal structure and differing size distributions between the stochastic and M96 aggregates likely explains the smaller DWR_{KaW} .

The polarimetric signals are similar, though the KDP peak is slightly weaker in the stochastic case ($5 \text{ }^{\circ} \text{ km}^{-1}$ for stochastic aggregates compared to $6 \text{ }^{\circ} \text{ km}^{-1}$ for the M96 aggregates) because both aggregates and crystals produce lower KDP values. Also, ZDR at heights smaller than 2 km is larger, saturating at 1 dB for the stochastic aggregates compared to 0.5 dB for the M96 aggregates. Looking at spectrally resolved ZDR (not shown), the larger ZDR is caused by the large aggregates populating the fast-falling side of the spectrum. These aggregates are not present in the M96 simulation.

Overall, the forward simulations reveal a pronounced effect of the stochastic formulation of aggregate snowflakes in *McSnow* on the Doppler spectra, multi-frequency and polarimetric radar quantities. A validation with actual radar observations is part of an ongoing research project, but beyond the scope of the current study.

6 Summary and Conclusions

This study presents a novel stochastic framework to describe the geometry of aggregate snowflakes within Monte Carlo Lagrangian particle models like *McSnow*. Unlike traditional deterministic or

empirically parameterized geometric representations of snowflakes, this approach leverages joint probability distributions derived from extensive datasets of simulated aggregates, generated using a detailed geometric aggregation model. These distributions are used to sample key microphysical and geometric variables: maximum dimension, aspect ratio, and area ratio. This method aims to capture the inherent variability and complexity observed in natural snowflakes, providing a more physically consistent description of their microstructure.

Another key improvement of this framework is its ability to model mixtures of monomer habits through a continuously defined metric of monomer habits of aggregates of mixtures. This enables flexible interpolation of geometric properties across populations dominated by different monomer types, such as plates, needles, and dendrites, thereby capturing the wide diversity in snowflake morphology observed in clouds. In the Lagrangian particle model, maximum dimension is treated as a pseudo-prognostic variable, dynamically updated during collision and depositional growth, while other geometric parameters like aspect ratio are assumed constant for aggregates during depositional growth. Some of these simplifications reflect the limits of our current knowledge of snowflake growth.

Idealized one-dimensional simulations of snowflake aggregation demonstrate that the inclusion of stochastic geometric variability enhances aggregational growth by increasing variability in particle terminal velocities. This leads to marginally larger aggregate sizes and somewhat reduced number and mass concentrations relative to models using classical empirical aggregate representations. These effects arise because geometric variability broadens the distribution of particle fall speeds, increasing the collision kernel and, consequently, the collision rate. Furthermore, case studies contrasting dendrite- and needle-dominated situations highlight the model's capability to represent distinct microstructural regimes, emphasizing its potential for improving microphysical realism in cloud-scale simulations.

Validation against in-situ observational datasets, particularly those collected by modern video disdrometers and imaging probes, is essential to rigorously assess the model's accuracy in representing snowflake microstructure and to quantify its implications for cloud microphysics and precipitation processes but is beyond the scope of the current study. Such validation would provide critical feedback for refining model assumptions, parameterizations, and identify missing physics.

Complementary to in-situ observations, we have shown that a validation of aggregate snowflake properties is possible through forward simulations of multi-frequency and polarimetric radar variables. Using a lookup table derived from DDA calculations of millions of stochastic aggregates, we simulated radar observables such as reflectivity, Doppler velocity, dual-wavelength ratios, and polarimetric moments across multiple frequencies and viewing geometries. These forward simulations reveal that the stochastic aggregate model reproduces key features seen in observed ice cloud profiles, while also producing broader Doppler spectra and more variable dual-wavelength signals than traditional empirical aggregate models. This highlights the diagnostic value of radar forward modeling for assessing aggregate variability and evaluating microphysical model performance against remote sensing data.

The framework currently assumes that each collision generates a new aggregate geometry independently, without memory of the parent particles' structure. However, since *McSnow* tracks detailed parent properties during collisions, it provides a natural foundation for incorporating structural memory in future models. Such memory-aware approaches could improve realism, though at the cost of increased complexity. Machine learning techniques may offer a path to reduce this cost by emulating high-dimensional memory effects.

Another open question is whether sticking efficiency depends on crystal habit. While dendritic particles are often assumed to aggregate more readily than plates due to their branched structure, direct observational evidence is scarce. Implementing habit-dependent sticking in *McSnow* would require empirical constraints from field or lab data.

More broadly, several key physical uncertainties remain: How long do aggregates take to settle into stable structures? Do branches break and re-freeze, leading to compaction or secondary ice production?

How does vapor deposition reshape aggregate geometry, and how does this depend on monomer habit and environmental conditions? Despite decades of research, many of these fundamental processes remain poorly understood, highlighting the need for continued observational and modeling efforts.

In conclusion, the stochastic aggregate snowflake framework developed here constitutes a significant advance toward capturing the natural variability and complexity of ice particle geometry in cloud microphysics models. By representing realistic geometric variability and enabling flexible treatment of monomer habit mixtures, this approach enhances predictive capability for simulating cloud microphysical processes and precipitation formation. Moreover, the framework provides a robust foundation for incorporating more sophisticated physical effects in the future, ultimately contributing to improved representation of ice microphysics in weather and climate models.

Acknowledgements

The study contributes to and is partly funded by the project FRAGILE of the SPP 2115 Fusion of Radar Polarimetry and Numerical Atmospheric Modelling Towards an Improved Understanding of Cloud and Precipitation Processes funded by the Deutsche Forschungsgemeinschaft (DFG 492234709). The authors would further like to thank Davide Ori for discussions about the performance of DDA calculations and orientations of ice particles.

References

Ball, P.: In retrospect: On the six-cornered snowflake, *Nature*, 480, <https://doi.org/10.1038/480455a>, 2011.

Basu, S. and Jones, C. E.: A Modified Lognormal Power-law Distribution for the Stellar Initial Mass Function, *Monthly Notices of the Royal Astronomical Society Letters*, 347, L47–L51, <https://doi.org/10.1111/j.1365-2966.2004.07341.x>, 2004.

Brath, M., Ekelund, R., Eriksson, P., Lemke, O., and Buehler, S. A.: Microwave and submillimeter wave scattering of oriented ice particles, *Atmos. Meas. Tech.*, 13, 2309–2333, <https://doi.org/10.5194/amt-13-2309-2020>, 2020.

Brdar, S. and Seifert, A.: McSnow: A Monte-Carlo Particle Model for Rimming and Aggregation of Ice Particles in a Multidimensional Microphysical Phase Space, *J. Adv. in Modeling Earth Systems*, 10, 187–206, <https://doi.org/10.1002/2017MS001167>, 2018.

Böhm, J. P.: A general hydrodynamic theory for mixed-phase microphysics. Part I: drag and fall speed of hydrometeors, *Atmos. Res.*, 27, 253 – 274, [https://doi.org/10.1016/0169-8095\(92\)90035-9](https://doi.org/10.1016/0169-8095(92)90035-9), 1992a.

Böhm, J. P.: A general hydrodynamic theory for mixed-phase microphysics. Part II: collision kernels for coalescence, *Atmos. Res.*, 27, 275 – 290, [https://doi.org/10.1016/0169-8095\(92\)90036-A](https://doi.org/10.1016/0169-8095(92)90036-A), 1992b.

Böhm, J. P.: A general hydrodynamic theory for mixed-phase microphysics. Part III: Rimming and aggregation, *Atmos. Res.*, 28, 103 – 123, [https://doi.org/10.1016/0169-8095\(92\)90023-4](https://doi.org/10.1016/0169-8095(92)90023-4), 1992c.

Chabrier, G.: Galactic Stellar and Substellar Initial Mass Function, *Publications of the Astronomical Society of the Pacific*, 115, 763–795, <https://doi.org/10.1086/376392>, 2003.

Chandrakar, K. K., Grabowski, W. W., Morrison, H., and Bryan, G. H.: Impact of Entrainment Mixing and Turbulent Fluctuations on Droplet Size Distributions in a Cumulus Cloud: An Investigation Using Lagrangian Microphysics with a Subgrid-Scale Model, *J. Atmos. Sci.*, 78, 2983 – 3005, <https://doi.org/10.1175/JAS-D-20-0281.1>, 2021.

Chellini, G. and Kneifel, S.: Turbulence as a Key Driver of Ice Aggregation and Rimming in Arctic Low-Level Mixed-Phase Clouds, Revealed by Long-Term Cloud Radar Observations, *Geophys. Res. Lett.*, 51, e2023GL106599, <https://doi.org/10.1029/2023GL106599>, 2024.

Connolly, P. J., Emersic, C., and Field, P. R.: A laboratory investigation into the aggregation efficiency of small ice crystals, *Atmos. Chem. Phys.*, 12, 2055–2076, <https://doi.org/10.5194/acp-12-2055-2012>, 2012.

Draine, B. T. and Flatau, P. J.: Discrete-dipole approximation for scattering calculations, *Journal of the Optical Society of America A*, 11, 1491–1499, <https://doi.org/10.1364/JOSAA.11.001491>, 1994.

Dunnavan, E. L.: How snow aggregate ellipsoid shape and orientation variability affects fall speed and self-aggregation rates, *J. Atmos. Sci.*, 78, 51–73, <https://doi.org/10.1175/JAS-D-20-0128.1>, 2021.

Dunnavan, E. L., Jiang, Z., Harrington, J. Y., Verlinde, J., Fitch, K., and Garrett, T. J.: The Shape and Density Evolution of Snow Aggregates, *J. Atmos. Sci.*, 76, 3919–3940, <https://doi.org/10.1175/JAS-D-19-0066.1>, 2019.

Gillespie, D. T.: An Exact Method for Numerically Simulating the Stochastic Coalescence Process in a Cloud, *J. Atmos. Sci.*, 32, 1977 – 1989, 1975.

Grabowski, W. W. and Wang, L.-P.: Growth of cloud droplets in a turbulent environment, *Annual review of fluid mechanics*, 45, 293–324, 2013.

Hales, T.: The Formal Proof of the Kepler Conjecture: a critical retrospective, *arXiv*, URL <https://arxiv.org/abs/2402.08032>, 2024.

Karrer, M., Seifert, A., Siewert, C., Ori, D., von Lerber, A., and Kneifel, S.: Ice Particle Properties Inferred From Aggregation Modelling, *J. Adv. in Modeling Earth Systems*, 12, e2020MS002066, <https://doi.org/10.1029/2020MS002066>, 2020.

Kneifel, S., von Lerber, A., Tiira, J., Moisseev, D., Kollias, P., and Leinonen, J.: Observed relations between snowfall microphysics and triple-frequency radar measurements, *J. Geophys. Res.*, 120, 6034–6055, <https://doi.org/https://doi.org/10.1002/2015JD023156>, 2015.

Köbschall, K., Breitenbach, J., Roisman, I. V., Tropea, C., and Hussong, J.: Geometric descriptors for the prediction of snowflake drag, *Exp. Fluids*, 64, 4, <https://doi.org/10.1007/s00348-022-03539-x>, 2023.

Leinonen, J. and Moisseev, D.: What do triple-frequency radar signatures reveal about aggregate snowflakes?, *J. Geophys. Res.*, 120, 229–239, 2015.

Leinonen, J. and Szyrmer, W.: Radar signatures of snowflake riming: A modeling study, *Earth and Space Science*, 2, 346–358, <https://doi.org/10.1002/2015EA000102>, 2015.

Leinonen, J., Grazioli, J., and Berne, A.: Reconstruction of the mass and geometry of snowfall particles from multi-angle snowflake camera (MASC) images, *Atmospheric Measurement Techniques*, 14, 6851–6866, <https://doi.org/10.5194/amt-14-6851-2021>, 2021.

Libbrecht, K. G.: Snow Crystals, *arXiv* preprint arXiv:1910.06389, <https://doi.org/10.48550/arXiv.1910.06389>, 2019.

Locatelli, J. D. and Hobbs, P. V.: Fall speeds and masses of solid precipitation particles, *J. Geophys. Res.*, 79, 2185–2197, <https://doi.org/10.1029/JC079i015p02185>, 1974.

Lu, Y., Jiang, Z., Aydin, K., Verlinde, J., Clothiaux, E. E., and Botta, G.: A polarimetric scattering database for non-spherical ice particles at microwave wavelengths, *Atmos. Meas. Tech.*, 9, 5119–5134, <https://doi.org/10.5194/amt-9-5119-2016>, 2016.

Mason, S. L., Hogan, R. J., Westbrook, C. D., Kneifel, S., Moisseev, D., and von Terzi, L.: The importance of particle size distribution and internal structure for triple-frequency radar retrievals of the morphology of snow, *Atmos. Meas. Tech.*, 12, 4993–5018, <https://doi.org/10.5194/amt-12-4993-2019>, 2019.

Mitchell, D. L.: Use of mass-and area-dimensional power laws for determining precipitation particle terminal velocities, *J. Atmos. Sci.*, 53, 1710–1723, [https://doi.org/10.1175/1520-0469\(1996\)053;1710:UOMAAD;2.0.CO;2](https://doi.org/10.1175/1520-0469(1996)053;1710:UOMAAD;2.0.CO;2), 1996.

Mitchell, D. L., Zhang, R., and Pitter, R. L.: Mass-dimensional relationships for ice particles and the influence of riming on snowfall rates, *J. Appl. Met.*, 29, 153–163, 1990.

Moisseev, D. N., Lautaportti, S., Tyynela, J., and Lim, S.: Dual-polarization radar signatures in snowstorms: Role of snowflake aggregation, *J. Geophys. Res.*, 120, 12,644–12,665, <https://doi.org/10.1002/2015JD023884>, 2015.

Morrison, H., van Lier-Walqui, M., Fridlind, A. M., Grabowski, W. W., Harrington, J. Y., Hoose, C., Korolev, A., Kumjian, M. R., Milbrandt, J. A., Pawlowska, H., et al.: Confronting the challenge of modeling cloud and precipitation microphysics, *J. Adv. in Modeling Earth Systems*, 12, e2019MS001689, 2020.

Morrison, H., Chandrakar, K. K., Shima, S.-I., Dziekan, P., and Grabowski, W. W.: Impacts of stochastic coalescence variability on warm rain initiation using Lagrangian microphysics in box and large-eddy simulations, *J. Atmos. Sci.*, 81, 1067–1093, 2024.

Onishi, R. and Seifert, A.: Reynolds-number dependence of turbulence enhancement on collision growth, *Atmos. Chem. Phys.*, 16, 12 441–12 455, <https://doi.org/10.5194/acp-16-12441-2016>, 2016.

Ori, D., von Terzi, L., Karrer, M., and Kneifel, S.: snowScatt 1.0: consistent model of microphysical and scattering properties of rimed and unrimed snowflakes based on the self-similar Rayleigh–Gans approximation, *Geosci. Model Dev.*, 14, 1511–1531, 2021.

Przybylo, V. M., Sulia, K. J., Lebo, Z. J., and Schmitt, C. G.: The Ice Particle and Aggregate Simulator (IPAS). Part II: Analysis of a Database of Theoretical Aggregates for Microphysical Parameterization, *J. Atmos. Sci.*, 79, 1633–1649, <https://doi.org/10.1175/JAS-D-21-0179.1>, 2022.

Seifert, A., Leinonen, J., Siewert, C., and Kneifel, S.: The Geometry of Rimed Aggregate Snowflakes: A Modeling Study, *J. Adv. in Modeling Earth Systems*, 11, 712–731, <https://doi.org/10.1029/2018MS001519>, 2019.

Shaw, R. A.: Particle-turbulence interactions in atmospheric clouds, *Annual Review of Fluid Mechanics*, 35, 183–227, 2003.

Shima, S.-i., Kusano, K., Kawano, A., Sugiyama, T., and Kawahara, S.: The super-droplet method for the numerical simulation of clouds and precipitation: A particle-based and probabilistic microphysics model coupled with a non-hydrostatic model, *Quart. J. Roy. Met. Soc.*, 135, 1307–1320, 2009.

Shima, S.-i., Sato, Y., Hashimoto, A., and Misumi, R.: Predicting the morphology of ice particles in deep convection using the super-droplet method: development and evaluation of SCALE-SDM

0.2. 5-2.2. 0,-2.2. 1, and-2.2. 2, *Geosci. Model Dev.*, 13, 4107–4157, <https://doi.org/10.5194/gmd-13-4107-2020>, 2020.

Telford, J. W.: A New Aspect of Coalescence Theory, *J. Atmos. Sci.*, 12, 436 – 444, 1955.

von Terzi, L., Dias Neto, J., Ori, D., Myagkov, A., and Kneifel, S.: Ice microphysical processes in the dendritic growth layer: a statistical analysis combining multi-frequency and polarimetric Doppler cloud radar observations, *Atmos. Chem. Phys.*, 22, 11 795–11 821, <https://doi.org/10.5194/acp-22-11795-2022>, 2022.

von Terzi, L., Ori, D., and Kneifel, S.: A Microwave Scattering Database of Oriented Ice and Snow Particles: Supporting Habit-Dependent Growth Models and Radar Applications (McRadar 1.0.0), EGUsphere [preprint], <https://doi.org/10.5194/egusphere-2025-3910>, 2025.

Welss, J.-N., Siewert, C., and Seifert, A.: Explicit habit-prediction in the Lagrangian super-particle ice microphysics model McSnow, *J. Adv. in Modeling Earth Systems*, 16, e2023MS003 805, 2024.

Westbrook, C., Ball, R., Field, P., and Heymsfield, A. J.: Theory of growth by differential sedimentation, with application to snowflake formation, *Physical Review E*, 70, 021 403, 2004a.

Westbrook, C. D., Ball, R. C., Field, P. R., and Heymsfield, A. J.: Universality in snowflake aggregation, *Geophysical Research Letters*, 31, <https://doi.org/10.1029/2004GL020363>, 2004b.

Yurkin, M. A. and Hoekstra, A. G.: The discrete dipole approximation: an overview and recent developments, *J. Quant. Spectrosc. Radiat. Transf.*, 106, 558–589, <https://doi.org/10.1016/j.jqsrt.2007.01.034>, 2007.

Yurkin, M. A. and Hoekstra, A. G.: The discrete-dipole-approximation code ADDA: capabilities and known limitations, *J. Quant. Spectrosc. Radiat. Transf.*, 112, 2234–2247, <https://doi.org/10.1016/j.jqsrt.2011.01.031>, 2011.